

Data-based theoretical identification of subcellular calcium compartments and estimation of calcium dynamics in cardiac myocytes

Leonid Livshitz¹, Karoly Acsai^{2,3}, Gudrun Antoons^{2,4}, Karin Sipido² and Yoram Rudy¹

¹Cardiac Bioelectricity and Arrhythmia Centre, Washington University in St Louis, St Louis, MO, USA

²Laboratory of Experimental Cardiology, University of Leuven, Leuven, Belgium

³Division of Cardiovascular Pharmacology, Hungarian Academy of Sciences, Szeged, Hungary

⁴Department of Cardiology, Medical University of Graz, Graz, Austria

Key points

- Ca^{2+} release from intracellular stores affects the cardiac action potential via currents through L-type Ca^{2+} channels (I_{Ca}) and the sodium/calcium exchanger (I_{NCX}).
- Dynamic interactions between released calcium, I_{Ca} and I_{NCX} occur in a restricted subcellular compartment, close to Ca^{2+} released sites, where calcium concentration (Ca_t) cannot be measured.
- We used a computational model and experimental data to define this compartment and to provide a theoretical basis for estimating Ca_t .
- We estimated Ca_t from recordings of I_{Ca} and I_{NCX} and optical recordings of whole-cell calcium concentration (Ca_m).
- Estimated peak Ca_t ranged from $6\ \mu\text{M}$ to $25\ \mu\text{M}$, depending on calcium load. Time to equilibrium between Ca_t and Ca_m was ~ 350 ms. The Ca_t values are in the range of I_{Ca} and I_{NCX} sensitivity to calcium, implying that there is significant effect of Ca^{2+} in this restricted domain on their kinetics and on the action potential during cell excitation.

Abstract In cardiac cells, Ca^{2+} release flux (J_{rel}) via ryanodine receptors (RyRs) from the sarcoplasmic reticulum (SR) has a complex effect on the action potential (AP). Coupling between J_{rel} and the AP occurs via L-type Ca^{2+} channels (I_{Ca}) and the $\text{Na}^+/\text{Ca}^{2+}$ exchanger (I_{NCX}). We used a combined experimental and modelling approach to study interactions between J_{rel} , I_{Ca} and I_{NCX} in porcine ventricular myocytes. We tested the hypothesis that during normal uniform J_{rel} , the interaction between these fluxes can be represented as occurring in two myoplasmic subcompartments for Ca^{2+} distribution, one (T-space) associated with RyR and enclosed by the junctional portion of the SR membrane and corresponding T-tubular portion of the sarcolemma, the other (M-space) encompassing the rest of the myoplasm. I_{Ca} and I_{NCX} were partitioned into subpopulations in the T-space and M-space sarcolemma. We denoted free Ca^{2+} concentrations in T-space and M-space Ca_t and Ca_m , respectively. Experiments were designed to allow separate measurements of I_{Ca} and I_{NCX} as a function of J_{rel} . Inclusion of T-space in the model allowed us to reproduce *in silico* the following important experimental results: (1) hysteresis of I_{NCX} dependence on Ca_m ; (2) delay between peak I_{NCX} and peak Ca_m during caffeine application protocol; (3) delay between I_{NCX} and Ca_m during Ca^{2+} -induced- Ca^{2+} -release; (4) rapid I_{Ca} inactivation (within 2 ms) due to J_{rel} , with magnitude graded as a function of the SR Ca^{2+} content; (5) time delay between I_{Ca} inactivation due to J_{rel} and Ca_m . Partition of 25% NCX in T-space and 75% in M-space provided the best fit to the experimental data. Measured Ca_m and I_{Ca} or I_{NCX} were used

as input to the model for estimating Ca_t . The actual model-computed Ca_t , obtained by simulating specific experimental protocols, was used as a gold standard for comparison. The model predicted peak Ca_t in the range of 6–25 μM , with time to equilibrium of Ca_t with Ca_m of ~ 350 ms. These Ca_t values are in the range of LCC and RyR sensitivity to Ca^{2+} . An increase of the SR Ca^{2+} load increased the time to equilibrium. The I_{Ca} -based estimation method was most accurate during the ascending phase of Ca_t . The I_{NCX} -based method provided a good estimate for the descending phase of Ca_t . Thus, application of both methods in combination provides the best estimate of the entire Ca_t time course.

(Received 30 January 2012; accepted after revision 23 April 2012; first published online 30 April 2012)

Corresponding author Y. Rudy: Cardiac Bioelectricity and Arrhythmia Centre, Washington University in St Louis, One Brookings Drive, St Louis 63130-4899, MO, USA. Email: rudy@wustl.edu

Abbreviations AP, action potential; CDI, Ca^{2+} -dependent inactivation; DAD, delayed afterdepolarization; EAD, early afterdepolarization; LCC, L-type Ca^{2+} channel; NCX, $3Na^+/Ca^{2+}$ exchanger; PMCA, plasmalemmal Ca^{2+} -ATPase pump; RDI, J_{rel} -dependent inactivation of I_{Ca} ; RyR, ryanodine receptor; SERCA, SR Ca^{2+} -ATPase pump; SR, sarcoplasmic reticulum; VDI, voltage-dependent inactivation of I_{Ca} .

Introduction

Ca^{2+} release flux (J_{rel}) from the sarcoplasmic reticulum (SR) via ryanodine receptors (RyRs) exerts a complex effect on the cardiac action potential (AP) via Ca^{2+} -dependent inactivation of L-type Ca^{2+} channels (LCCs) (repolarizing effect) and activation of $3Na^+/Ca^{2+}$ exchangers (NCXs) (depolarizing effect). It has been shown that abnormality of J_{rel} due to genetic defects in RyR, heart failure, or excessive phosphorylation during exercise and stress could cause abnormal cellular electrical activity and arrhythmic behaviour. For example (1) beat-to-beat alternans in J_{rel} is associated with arrhythmogenic AP alternans, with amplitude that depends on the balance between Ca^{2+} flux via LCCs (I_{Ca}) and NCX (I_{NCX}); this process is modulated by the Ca^{2+} /calmodulin-dependent protein kinase II (CAMKII) (Sato *et al.* 2006, Livshitz & Rudy, 2007); (2) I_{Ca} recovery from Ca^{2+} -dependent inactivation following J_{rel} is implicated in the development of early afterdepolarizations (EADs) (Antoons *et al.* 2007); and (3) diastolic J_{rel} underlies the formation of delayed afterdepolarizations (DADs) and triggered activity at high levels of β -adrenergic tone (e.g. Belevych *et al.* 2011; Priori & Chen, 2011).

The mechanism of coupling between J_{rel} , I_{NCX} , I_{Ca} and the AP is not completely understood, even under normal physiological conditions. Consensus exists that the interactions are mediated by the free Ca^{2+} sensed by these channels, and are modulated by the CaMKII signalling pathway. However, optical recordings of the whole-cell (global) Ca^{2+} transient (Ca_m) show dynamics which correlate poorly with the much faster kinetics of the ionic currents (I_{Ca} and I_{NCX}). This implies that these channels are experiencing different local Ca^{2+} transients (Ca_t) that cannot be measured with current experimental techniques with sufficient

temporal and spatial resolution. Consequently, combined experimental/computational methods were developed for estimating local Ca^{2+} from measurements of whole-cell Ca^{2+} using fluorescence imaging, together with recorded I_{NCX} (Egan *et al.* 1989; Trafford *et al.* 1995; Weber *et al.* 2001) or I_{Ca} (Sipido *et al.* 1995; Sham, 1997; Zahradnikova *et al.* 2004; Antoons *et al.* 2007) as local Ca^{2+} sensors (reporters). Early work used Ca_m and mathematical modelling to calculate J_{rel} in skeletal (Melzer *et al.* 1987) and cardiac (Sipido & Wier, 1991) fibres. These indirect (inverse) methods for estimating local Ca^{2+} from I_{NCX} and I_{Ca} recordings rely heavily on the mathematical models employed and the quality of recorded I_{NCX} and I_{Ca} data.

Due to tight coupling between Ca^{2+} cycling and membrane voltage (V) in cardiac myocytes, it is difficult to control I_{NCX} and I_{Ca} independently and separate Ca^{2+} -dependent from V -dependent processes in experiments. For example, it is extremely challenging to separate effects of Ca^{2+} -dependent (CDI) and voltage-dependent (VDI) inactivation of I_{Ca} , or effects of Ca^{2+} -dependent and voltage-dependent modulation of I_{NCX} . In addition, modulation of I_{Ca} by Ca^{2+} is due to both CDI and changes in the driving force. Moreover, there is strong interaction (mediated by Ca^{2+} changes) between I_{Ca} and I_{NCX} during an AP and therefore caution should be taken in extrapolating estimates of local Ca^{2+} from each individual current to the physiological environment of the myocyte during excitation. Ca^{2+} fluxes have been measured under experimental conditions (voltage clamp, dialysed whole cell, cocktails of blockers, non-physiological ion concentrations, artificial ion buffers, non-physiological levels of protein phosphorylation, etc.) which differ from those in intact functioning cardiac cells. Additional complexity arises from the fact that different cardiac cells (e.g. ventricular, atrial, purkinje) exhibit distinct structural organization, which is also age and species

dependent (Bootman *et al.* 2006; Soeller *et al.* 2007, 2009; Li & Rudy, 2011).

In ventricular myocytes, RyRs, NCXs and LCCs are distributed non-uniformly (Fig. 1A) in the SR membrane (RyRs) and sarcolemma (NCXs and LCCs) (Pasek *et al.* 2008; Jayasinghe *et al.* 2009; Smyrniasa *et al.* 2010). Not all LCCs and only a fraction of NCXs sense the same Ca^{2+} as RyRs (Adachi-Akahane *et al.* 1996), underscoring the importance of considering subcellular compartments for Ca^{2+} dynamics in mathematical models of the cell. Experimental data and model simulations suggest that Ca^{2+} flux per unit time through LCCs and RyRs is several orders of magnitude greater than the diffusion flux towards the core of the cell, resulting in local subcellular Ca^{2+} gradients (Allbritton *et al.* 1992). In addition, local Ca^{2+} buffers contribute to a relatively slow (tens of milliseconds) dissipation of these Ca^{2+} gradients (Naraghi & Neher, 1997; Higgins *et al.* 2007).

Unfortunately, using numerical models of the reaction-diffusion system in the realistic, detailed geometry of the cell requires precise knowledge of the intracellular structure and of Ca^{2+} diffusion properties in this structure. It involves many parameters that cannot be constrained precisely and is computationally very demanding (e.g. Chen-Izu *et al.* 2006; Soeller *et al.* 2009).

The representation of spatial organization in a compartmental model is a simplification that makes computation possible (Atkins, 1969). It has been used extensively in modelling calcium cycling in cardiac myocytes (Standen & Stanfield, 1982; Adler *et al.* 1985; Luo & Rudy, 1994). Here, we use this approach to better define functional cellular compartments for Ca^{2+} interactions and to provide a theoretical basis for estimation of dynamic Ca^{2+} concentrations in these compartments. We hypothesize that under normal physiological conditions (i.e. uniform whole cell J_{rel}), the interaction between J_{rel} , I_{Ca} and I_{NCX} can be formulated, to a very good approximation, as occurring in four functional compartments of Ca^{2+} distribution, two in the myoplasm and two in the SR. One myoplasmic compartment (denoted T-space) is associated structurally with the RyRs and enclosed by the tubular portion of the sarcolemma and the junctional portion of the SR membrane (enclosed by the dashed curve in Fig. 1A). The other myoplasmic compartment (M-space) encompasses the rest of the myoplasm, enclosed by the non-tubular sarcolemma and non-junctional SR membrane. LCCs and NCXs are present in the sarcolemma of both T-space and M-space, but with different density in each compartment. We denote free Ca^{2+} concentrations in T and M spaces Ca_t and Ca_m , respectively. Similarly, the SR is also divided into two compartments of Ca^{2+} distribution. One compartment (denoted J-space) is associated structurally with the RyRs and the junctional portion of the SR membrane. The other compartment (N-space) encompasses the rest of SR

(network SR) as we have done previously (Luo & Rudy, 1994). We employ mathematical modelling together with experimental measurements to explore the interactions of J_{rel} , I_{Ca} and I_{NCX} in the T-space and to provide a theoretical basis for estimating the Ca_t dynamic properties in this functional space, where J_{rel} , I_{Ca} and I_{NCX} interact.

The choice of compartments was dictated by the assumptions of a uniform Ca^{2+} distribution in each compartment and a spatially uniform Ca^{2+} flux between communicating compartments. It was guided by structural and functional considerations and differs from 'subspace' and 'bulk myoplasm' used in many previous compartmental models. In these models, 'subspace' has been used to define a continuous subsarcolemmal space in the entire cell. In certain models, it was subdivided to contain a 'dyadic' space (Shannon *et al.* 2004; Higgins *et al.* 2007; Mahajan *et al.* 2008); the dyadic space communicated with the subsarcolemmal subspace, which in turn communicated with the bulk myoplasm. This implies that dyads are distributed uniformly beneath the sarcolemma, and all NCXs are affected identically by J_{rel} via a Ca^{2+} diffusion flux from the dyadic space. Based on structural and functional properties, including the non-uniform distribution and partition of LCCs and NCXs between T-tubular and non-T-tubular portions of the sarcolemma, and of RyRs in the SR membrane, Ca^{2+} distribution cannot be assumed uniform in a subsarcolemmal 'subspace' compartment. Rather, RyRs interact with LCCs and NCXs in a functional compartment near the RyR, which we label T-space. Figure 1 depicts two populations of LCCs and NCXs, one interacting with RyRs in the T-space (via a common pool of Ca^{2+} , Ca_t), and the other communicating directly with the M-space. Based on experimental data, we estimate the fraction of NCXs that are coupled functionally to RyRs via Ca_t .

Methods

Symbols and definitions are given in Table 1.

Ethical approval

All experiments were conducted at the University of Leuven, Belgium, according to the *Guide for the Care and Use of Laboratory Animals* of the National Institutes of Health (USA). Experimental protocols were approved by the ethical committee of the University of Leuven. The current study conforms to the ethical standards set by *The Journal of Physiology* (Drummond, 2009). Killing of the pigs was done under full anaesthesia (premedication with tiletamine and zolazepam, 4 mg kg⁻¹ i.m. and xylazine 0.25 mg kg⁻¹ i.m., maintenance anaesthesia with propofol i.v., 7 mg kg⁻¹ h⁻¹); pigs were intubated and ventilated with a 1:1 oxygen-air mixture. After an additional bolus

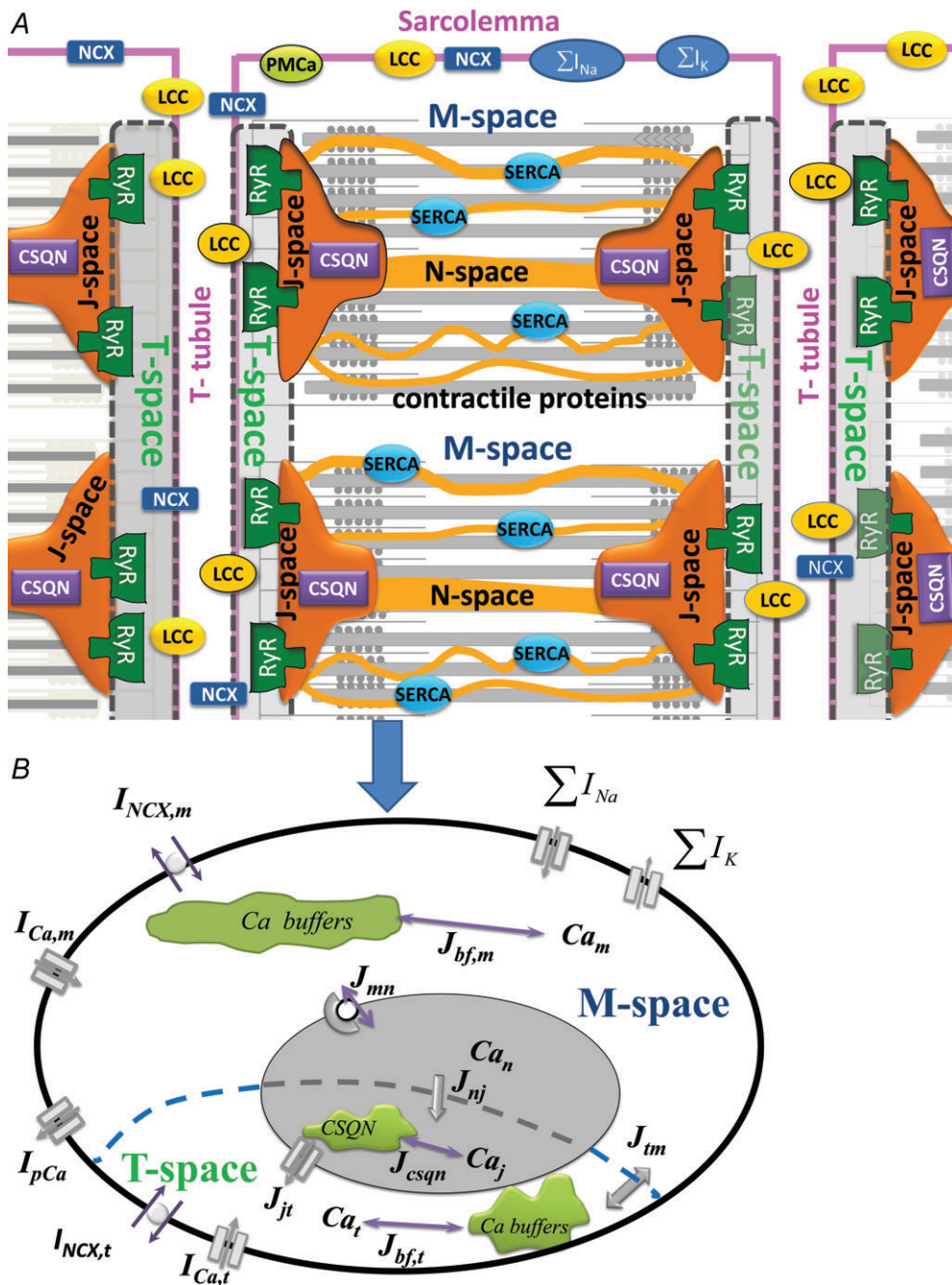


Figure 1. Compartmental model of Ca²⁺ cycling, based on structural organization of a ventricular myocyte

A, schematic diagram of the structural organization of a ventricular myocyte. Sarcolemmal Ca²⁺-ATPase (PMCa), L-type Ca²⁺ channels (LCC), 3Na⁺/Ca²⁺ exchanger (NCX) and Ca²⁺ binding proteins (buffers) are expressed throughout the sarcolemma. T-Tubules run radially and flank each sarcomere. Ca²⁺ release channels (RyRs) are expressed in the junctional portion of the SR membrane which faces the T-tubular portion of the sarcolemma and bounds the calsequestrin (CSQN) containing J-spaces. The junctional portion of the SR membrane and corresponding T-tubular portion of the sarcolemma form the T-spaces (grey spaces enclosed by dashed boundaries). During uniform activation of all RyR, identical Ca²⁺ distribution can be assumed in all J-spaces and in all T-spaces. Given the structural periodicity of the myocyte, a cell average Ca²⁺ concentration in J-space (Ca_j) and T-space (Ca_t) can be defined. SR Ca²⁺-ATPase (SERCA) is expressed in the network portion of the SR membrane which encloses the N-space. M-space is separated by the network portion of the SR membrane from the N-space and contains Ca²⁺ sensitive contractile (troponin) and regulatory (calmodulin) proteins. ΣI_K and ΣI_{Na} are sum of trans-sarcolemmal K⁺ and Na⁺ fluxes, respectively. B, compartmental model of Ca²⁺ cycling

Table 1. Symbols and definitions

V	Transmembrane potential	mV
Ca_t	Free Ca^{2+} concentration in T-space	mm
\overline{Ca}_t	Inverse estimated Ca_t	
Ca_m	Free Ca^{2+} concentration in M-space	
Ca_j	Free Ca^{2+} concentration in junctional SR (J-space)	mm
Ca_n	Free Ca^{2+} concentration in network SR (N-space)	mm
Ca_{cmdn}	Ca^{2+} bound to calmodulin in M-space	mm
Ca_{csqn}	Ca^{2+} bound to calsequestrine in J-space	mm
Ca_{trpn}	Ca^{2+} bound to troponin in M-space	mm
$Ca_{b,f}$	Ca^{2+} bound to fast buffer in T-space	mm
$Ca_{b,s}$	Ca^{2+} bound to slow buffer in T-space	mm
$J_{Ca,m}$	Trans-sarcolemmal Ca^{2+} flux in M-space	mm ms^{-1}
$J_{Ca,t}$	Trans-sarcolemmal Ca^{2+} flux in T-space	mm ms^{-1}
J_{nj}	Ca^{2+} between N-space to J-space	mm ms^{-1} s
τ_{tr}	Time constant of J_{nj}	ms
J_{tm}	Ca^{2+} flux between T-space and M-space	mm ms^{-1} s
τ_{diff}	Time constant of J_{tm}	ms
J_{mn}	Ca^{2+} flux between M-space and N-space	mm ms^{-1}
AP	Action potential	
I_{Ca}	L-type Ca^{2+} current	$\mu A \mu F^{-1}$
f_{Ca}	Ca^{2+} -dependent inactivation gate of I_{Ca}	
\overline{f}_{Ca}	Inverse estimated f_{Ca}	
β	Fraction of NCX in T-space	
I_{NCX}	Na^+ - Ca^{2+} exchanger current	$\mu A \mu F^{-1}$
NCX_{max}	Maximal turnover rate of I_{NCX}	$\mu A \mu F^{-1}$
K_{NCX}	I_{NCX} affinity to Ca^{2+}	mm
I_{Ca}^0	I_{Ca} in the absence of J_{rel}	$\mu A \mu F^{-1}$
$\Delta I_{Ca} = I_{Ca} - I_{Ca}^0$	Difference current (presence-absence of J_{rel})	
t_{max}	Time of maximal ΔI_{Ca}	ms
I_{pCa}	Ca^{2+} current via PMCA	$\mu A \mu F^{-1}$
I_{Cab}	Background Ca^{2+} current	$\mu A \mu F^{-1}$
J_{rel}	Ca^{2+} flux via RyRs	mm ms^{-1}
$\sum I_{Na}$	Sum of transsarcolemmal Na^+ fluxes	mm ms^{-1}
$\sum I_K$	Sum of transsarcolemmal K^+ fluxes	mm ms^{-1}
J_{SERCA}	Ca^{2+} flux via SERCA	mm ms^{-1}
J_{leak}	Ca^{2+} leak flux from J-space	mm ms^{-1}
$J_{b,x}$	Ca^{2+} flux from and to Ca^{2+} buffers 'x'	mm ms^{-1}
V_x	Volume of compartment 'x'	μl
C_m, C_t	M-space and T-space capacitances of sarcolemma, μF	
F	Faraday constant, 96,487 C mol^{-1}	
R	Gas constant, 8314 J $mmol^{-1} K^{-1}$	
T	Temperature, 310 K	
Na_o	External Na^+ concentration	
Ca_o	External Ca^{2+} concentration	

based on the structural organization in panel A, when synchronized activation of RyR generates a uniform Ca^{2+} flux (J_{jt}) from J-space to T-space. The transsarcolemmal Ca^{2+} fluxes, which include currents via LCC (I_{Ca}) and NCX (I_{NCX}), are partitioned between T-space and M-space. The effects of the contractile and regulatory proteins on Ca^{2+} dynamics is accounted for by buffering fluxes in the M-space ($J_{bf,m}$), T-space ($J_{bf,t}$), and J-space (J_{csqn}). Ca^{2+} flux between M-space and N-space (J_{mn}) is carried by SERCA. Transfer of Ca^{2+} between T-space and M-space (J_{tm}) is proportional to the difference between Ca_t and Ca_m . Similarly, J_{nj} is proportional to the difference between Ca_n and Ca_j . Additional symbols are defined in the text. Computer code is available on the website <http://rudylab.wustl.edu/research/cell/lrd2.htm>.

of pentobarbital (100 mg kg⁻¹ I.M.), hearts were excised quickly and placed in oxygenated Tyrode solution.

Experimental considerations

The experiments were conducted in porcine ventricular myocytes and described in detail in Acsai *et al.* (2011). Briefly, experiments were designed to allow separate measurements of I_{Ca} and I_{NCX} as a function of J_{rel} , which was controlled by regulation of SR Ca²⁺ load using caffeine and voltage-clamp protocols. Whole-cell Ca²⁺ was measured optically. The size of the T-space compartment is orders of magnitude smaller than that of the M-space. Therefore, contribution from Ca_t to the optically measured Ca²⁺ signal can be regarded as negligible and the cell-average Ca²⁺ signal reflects Ca_m. The experimental protocols were conducted under voltage clamp conditions, with all ion concentrations, except Ca²⁺, maintained constant. In addition, we utilized a depolarizing step to +10 mV which ensures maximal spatially uniform activation of J_{rel} to reflect normal conditions in non-failing myocytes (see Fig. 2A in Acsai *et al.* 2011). In addition, large concentrations of caffeine were used (10 mM) to ensure spatial uniformity of caffeine-evoked J_{rel} . Also, the state of the cell (SR Ca²⁺ load, depolarizing V pulses) in both the I_{Ca} and I_{NCX} experiments was identical to yield identical estimations of Ca_t. Experimental recordings of I_{Ca} , Ca_m and I_{NCX} were used as an input to the model for estimating Ca_i; the mathematical formulation and simulation procedures are described below.

Myocyte isolation. In the current study we used ventricular myocytes isolated from the mid-myocardial layer of the posterior wall of healthy pigs. Animals ($n = 12$, weight 35–45 kg) were housed and treated according to the *Guide for the Care and Use of Laboratory Animals* (National Institutes of Health, USA) and experimental protocols were approved by the in-house ethical committee at the University of Leuven. Killing of the pigs was done under full anaesthesia, hearts were excised quickly and placed in oxygenated Tyrode solution. The circumflex coronary artery was cannulated and the myocardium was perfused with Ca²⁺-free Tyrode solution and subsequently enzyme solution. Isolated cells were stored at room temperature and used within 12 h. The isolation procedure was as described before (Heinzel *et al.* 2002).

Chemical solutions. Chemicals were purchased from Sigma, fluorescent probes from Invitrogen, Belgium. Tyrode solution for cell storage contained (in mM) NaCl 130, KCl 5.4, Hepes 11.8, MgCl₂ 0.5, CaCl₂ 1.8, and glucose 10, pH 7.40 with NaOH. For recording I_{CaL} and I_{NCX} , the extracellular solution contained (in mM): NaCl

130, CsCl 10, Hepes 11.8, MgCl₂ 0.5, CaCl₂ 1.8, glucose 10, pH 7.4 adjusted with NaOH. To block the fast Na⁺ current, 200 μM lidocaine was included in the external solution. In order to increase the amplitude of the I_{CaL} and facilitate study of Ca²⁺-dependent inactivation and recovery by increasing SR Ca²⁺ content, 5 μM forskolin was added to the external solution. The pipette solution contained (in mM): caesium aspartate 120, TEACl 10, NaCl 5, Hepes 10, MgCl₂ 0.5, MgATP 5, pH 7.2 adjusted with CsOH with 50 μM K5Fluo-3 was added as a fluorescent Ca²⁺ indicator for measurement of the global cytosolic Ca²⁺ concentration. In the experiments carried out in Na⁺ free conditions, the external solution contained *N*-methyl-D-glucamine 120, TEACl 20, Hepes 11, MgCl₂ 0.5, CaCl₂ 1.8, glucose 10, pH 7.4 with HCl.

Cardiac myocytes were placed in a perfusion chamber on an inverted microscope (Nikon Diaphot). The set-up for epifluorescence recording, calibration of the Ca²⁺-dependent fluorescence and measurement of membrane currents were as described previously (Acsai *et al.* 2011). Fluorescence signals were recorded from the entire cell and calibrated to [Ca²⁺] after obtaining F_{max} at the end of the experiments. All experiments were performed at 36°C.

Model geometry and calcium compartments

Typical spatial organization of a non-failing ventricular myocyte is shown in Fig. 1A. The cell membrane (sarcolemma) invaginates to form transverse tubules (T-tubule) which run predominantly radially across the muscle fibre. These tubules are situated between the sarcomeres, which consist of a regular array of Ca²⁺ binding myofilaments, forming the basic unit of the contractile machinery (Adrian, 1983; Bootman *et al.* 2006). Given the structural periodicity of the myocyte, only two sarcomeres in the radial direction (out of many) are shown. Approximately half of the sarcolemmal surface area is associated with the T-tubular system, where LCCs and NCXs are expressed at higher density. Ca²⁺-binding calsequestrin (CSQN) and RyRs are expressed in the J-space membrane and lumen, respectively. SR Ca²⁺-ATPase (SERCA) is expressed in the N-space membrane, in close proximity to the contractile proteins in the myoplasm.

When all RyRs are activated in synchrony to generate J_{rel} flux from J-spaces to T-spaces, uniform Ca²⁺ distributions can be assumed in these compartments and represented in the model by average Ca_j and Ca_t (Fig. 1A and B).

Compartmental model based on structural organization of a ventricular myocyte

A schematic diagram of the model is shown in Fig. 1B. The Luo–Rudy dynamic (LRd) model (Luo & Rudy,

1994) was used as the template for modelling Ca^{2+} cycling; it was modified to fit porcine data, as experiments were conducted in porcine myocytes. The LRd model includes three intracellular Ca^{2+} compartments (myoplasm, network SR and junctional SR). Each compartment is characterized functionally by the bound and free Ca^{2+} concentrations, and Ca^{2+} fluxes in and out of the compartment (Hund & Rudy, 2004; Faber *et al.* 2007). Bound Ca^{2+} in each compartment is associated with endogenous Ca^{2+} buffers. For the purpose of this study (and to better represent the structural organization of a ventricular myocyte), the original myoplasmic Ca^{2+} compartment of the LRd model was subdivided into two compartments: T-space and M-space (Fig. 1B). Following Winka *et al.* (1999), we assumed that SR calcium is divided between two functionally discrete pools, one is available for release during normal I_{Ca} -triggered J_{rel} (J-space), while the other is releasable by caffeine application but unavailable for release during normal triggered release (N-space).

Also, note that the T-space is not separated by a membrane from the M-space (nor is J-space from N-space); rather, they are separated functionally by Ca^{2+} diffusion barriers which result in faster and larger Ca^{2+} transients in the T-space (J-space) than in the M-space (N-space). Ca^{2+} diffusion barriers between T-space and M-space and between J-space and N-space (dashed curve, Fig. 1B) are accounted for by diffusion fluxes J_{tm} and J_{nj} , respectively.

The mathematical model

Free Ca^{2+} concentration (mM) in T-space, M-space, N-space and J-space are denoted Ca_t , Ca_m , Ca_n and Ca_j , respectively. Ca^{2+} efflux from compartment 'x' to compartment 'y' (J_{xy}) has units of millimolar of x volume (v_x) per ms. Consequently, to ensure Ca^{2+} conservation, Ca^{2+} influx into compartment y is normalized by the volume fractions $v_{xy} = v_x/v_y$. The balance of fluxes for each compartment in terms of free Ca^{2+} concentrations is as follows:

$$\begin{aligned} \frac{d\text{Ca}_t}{dt} &= J_{\text{Ca},t} + v_{jt} \cdot J_{jt} - J_{\text{tm}} - J_{\text{bf},t} \\ \frac{d\text{Ca}_m}{dt} &= J_{\text{Ca},m} + v_{\text{tm}} \cdot J_{\text{tm}} - J_{\text{mn}} - J_{\text{bf},m} \\ \frac{d\text{Ca}_n}{dt} &= v_{\text{mn}} \cdot J_{\text{mn}} - J_{\text{nj}} \\ \frac{d\text{Ca}_j}{dt} &= v_{\text{nj}} \cdot J_{\text{nj}} - J_{jt} - J_{\text{csqn}} \end{aligned} \quad (1)$$

where subscripts t, m, n, and j indicate the corresponding quantities for T-space, M-space, N-space and J-space, respectively. Trans-sarcolemmal Ca^{2+} fluxes into M-space and T-space are denoted

$J_{\text{Ca},m} = \psi_m(I_{\text{Ca},m} + I_{\text{Cab},m} + I_{\text{pCa},m} - 2I_{\text{NCX},m})$ and $J_{\text{Ca},t} = \psi_t(I_{\text{Ca},t} + I_{\text{Cab},t} + I_{\text{pCa},t} - 2I_{\text{NCX},t})$, respectively. $\psi_m = -C_m/(2v_mF)$ and $\psi_t = -C_t/(2v_tF)$ are Ca^{2+} current to flux conversion factors for T-space and M-space, respectively. $F = 96,485$ is the Faraday constant. Membrane capacitance in M-space (C_m) and T-space (C_t) is the same. I_{pCa} is current via PMCA (plasma membrane ATPase) and I_{Cab} is background leak current (Livshitz & Rudy, 2009).

M-space and T-space, and N-space and J-space communicate via diffusion fluxes, $J_{\text{tm}} = (\text{Ca}_t - \text{Ca}_m)/\tau_{\text{diff}}$ ($v_{\text{tm}} = v_t/v_m \approx 0.0152$) and $J_{\text{nj}} = (\text{Ca}_n - \text{Ca}_j)/\tau_{\text{tr}}$ ($v_{\text{nj}} = v_n/v_j \approx 11.5$), respectively. Ca^{2+} flux between J-space and T-space (J_{jt}) has two components, J_{rel} and J_{leak} . Formulations of these fluxes are provided in the Appendix eqn (A2).

Ca^{2+} binding sites (buffers) are defined in terms of Ca^{2+} fluxes between a buffer and its corresponding compartment ($J_{\text{bf},m}$, $J_{\text{bf},t}$ and J_{csqn} in Fig. 1B). In M-space, $J_{\text{bf},m}$ includes a fast component (calmodulin) and a slow component (troponin). Similarly, $J_{\text{bf},m}$ in T-space has fast ($J_{\text{b},f}$) and slow ($J_{\text{b},s}$) Ca^{2+} anionic binding sites. J_{mn} is carried by SERCA. Formulations of fluxes are provided in the Appendix eqns (A1)–(A3).

Parametrization of the model. Experimental data were used to fit the model parameters, including the activation and inactivation kinetics of I_{Ca} , partition of NCX between the T and M spaces, density of Ca^{2+} binding sites on the SR membrane and sarcolemma, calmodulin partition between the T and M compartments, and intra-compartmental Ca^{2+} diffusion rates. Whenever possible, we used different sets of experimental data for the forward model validation and for inverse model estimation. The parameter τ_{tr} (200–600 ms) was set to reproduce experimentally measured Ca_m restitution (Luo & Rudy, 1994). The time constant of Ca^{2+} flux between the T-space and M-space was fitted to reproduce the experimentally observed delay between peak Ca_m and the onset of I_{Ca} inactivation due to J_{rel} . The parameter τ_{diff} (0.1–0.2 ms) and T-space buffering parameters were set to reproduce the experimentally measured rate of rise of Ca_m (4–8 mM ms⁻¹, as in Sipido & Wier (1991)) and its time to peak. Several model parameters, such as compartment volumes and total concentrations of Ca^{2+} buffers, were constrained by conservation of total Ca^{2+} in the cell.

The state variables of the model are membrane voltage, free ion concentrations, and ion channels gating variables. Computation of ionic currents (e.g. I_{Ca} and I_{NCX}) from these state variables constitutes a forward problem. Estimation of Ca_t (the estimate is denoted $\overline{\text{Ca}}_t$) from Ca_m together with I_{Ca} or I_{NCX} constitutes an inverse problem (Keller, 1976). Note that Ca_m , I_{Ca} or I_{NCX} can be either measured experimentally or generated by the model in a

forward simulation. In the approach presented here, the forward-calculated Ca_t (obtained by simulating specific experimental protocols *in silico*) is used as a standard for comparison and evaluation of $\overline{Ca_t}$. This allows us to critically validate and evaluate different experimental methods and protocols that have been used to estimate Ca_t .

It should be noted that the sensitivity of the inverse model to variations in parameter values is much greater than that of the forward model, especially at saturating levels of Ca^{2+} .

Current through L-type Ca^{2+} channels, I_{Ca} . LCCs were partitioned between the T-space and M-space, with a large fraction (85–95%) in T-space; total $I_{Ca} = I_{Ca,m} + I_{Ca,t}$. We assumed that the intrinsic LCC properties are independent of their location and dropped the subscripts *m* and *t* for notational convenience. The L-type channel current is as in Luo & Rudy (1994):

$$I_{Ca} = P_{Ca} E_{Ca} d \cdot f \cdot f_{Ca} \quad (2)$$

where P_{Ca} is the maximal conductance, d is a V -dependent activation gate, f is a V - and Ca^{2+} -dependent inactivation gate, and f_{Ca} is a Ca^{2+} -dependent inactivation gate. E_{Ca} denotes the driving force for Ca^{2+} flux through the LCC as a function of trans-sarcolemmal Ca^{2+} and V gradients, given by the Goldman–Hodgkin–Katz relation (GHK) (Hille, 2001),

$$E_{Ca} = 4V\varphi F(Ca\gamma_{Ca}e^{V\varphi} - \gamma_{Ca0}Ca_0)/(e^{V\varphi} - 1) \quad (3)$$

where $\varphi = F/R/T = 0.0374$ (V^{-1}), $R = 8314$ ($J\ mol^{-1}\ K^{-1}$) is the universal gas constant, $T = 310$ is the absolute temperature (K), and γ_{Ca} and γ_{Ca0} are activity coefficients for free intracellular (Ca) and extracellular (Ca_0) concentrations, respectively. By definition $\gamma_{Ca_i} > \gamma_{Ca_o}$ if $Ca < Ca_0$. $\gamma_{Ca}Ca_i$ can be viewed as an effective concentration of Ca^{2+} (Hille, 2001). I_{Ca} inactivation is represented by the product of two time-dependent processes: (1) voltage-dependent inactivation modulated by free Ca^{2+} ions, f -gate, and (2) a Ca^{2+} -dependent process, f_{Ca} -gate.

Steady-state voltage dependence of I_{Ca} activation (d -gate). Formulation of the voltage-dependent activation d -gate was derived using peak values of I_{Ca} measured in porcine ventricular myocytes (Stengl *et al.* 2010). I_{Ca} elicited by test voltage pulses was normalized by the driving force E_{Ca} (eqn (3)) at each voltage step. A best-fit analytical expression for steady-state d_{∞} was obtained using the Matlab (The Mathworks, Natick, MA,

USA) subroutine ‘lsqcurvefit’ and is as follows:

$$d_{\infty} = I_{Ca,peak}/E_{Ca} \\ = \frac{1}{(1 + e^{-(V-16)/13.6})(1 + e^{-(V+5.97)/5.15})} \quad (4)$$

Supplemental Fig. S1A shows simulated (continuous trace) and measured (circles) I – V curves. Supplemental Fig. S1B shows model simulated d_{∞} (eqn (4), continuous black curve). Ca^{2+} was set to $0.1\ \mu M$ in these simulations. The time constant of I_{Ca} activation, τ_d , is fast and was set to its average value of 1 ms (Luo & Rudy, 1994).

Steady-state dependence of f -gate on V and Ca^{2+} . Following Morad & Soldatov (2005) we assumed that I_{Ca} inactivation is V -dependent and is not complete in the absence of Ca^{2+}

$$f_{\infty} = (1 - a_v)f_{V\infty} - a_v f_{V_{Ca\infty}} \\ = \frac{(1 - a_v)}{1 + e^{(V+32)/8}} + a_v - \frac{a_v}{1 + Ca_i/K_{V_{Ca}}} \quad (5)$$

$0 < a_v < 1$ is a factor that defines the contribution of Ca^{2+} ($f_{V_{Ca\infty}}$) and voltage ($f_{V\infty}$) to steady-state f_{∞} . Typically, a_v was set to 0.25. $f_{V\infty}$ and $f_{V_{Ca\infty}}$ are saturating functions of V and Ca^{2+} , respectively. $K_{V_{Ca}} = 3$ – $5\ \mu M$ is a half-saturation coefficient. Supplemental Fig. S1B shows measured (circles) and simulated (grey curve) $f_{V\infty}$ (Stengl *et al.* 2010). Note that a_v was set to 0 in this simulation.

Time-constant of I_{Ca} inactivation (τ_f) with Ca^{2+} -dependent acceleration. We assumed that I_{Ca} inactivation is V dependent and is accelerated in the presence of Ca^{2+} :

$$\tau_f = \tau_{fV} - \tau_{fV_{Ca}} = 66 + \frac{(V - 8.73)^2}{11.72 + 0.05V} - \frac{Ca_{V\tau}}{1 + K_{V_{\tau Ca}}/Ca_i} \quad (6)$$

$\tau_{fV_{Ca}}$ is a Ca^{2+} -dependent acceleration factor; its maximal value equals $Ca_{V\tau} = 55$ ms, and half-saturation constant $K_{V_{\tau Ca}} = 1\ \mu M$. The best fit of τ_f (V -dependent term in eqn (6)) to experimental data is shown in Supplemental Fig. S1C. In the simulations, τ_f values beyond experimentally recorded voltages (i.e. more than 40 mV and less than -10 mV) were set to 143 ms and 95 ms, respectively. $Ca_{V\tau}$ was set to zero in the simulation of Fig. S1C.

Ca^{2+} -dependent inactivation gate f_{Ca} . Steady-state ($f_{Ca\infty}$) and time constant (τ_{fCa}) of Ca^{2+} -dependent inactivation were formulated as follows:

$$f_{Ca_i,\infty} = \frac{1}{1 + Ca_i/K_{fCa}}, \\ \tau_{fCa} = \frac{0.2}{0.01 + 4Ca_i} + \frac{0.1}{4 + 0.01/Ca_i} \quad (7)$$

where $K_{fCa} = 4 \mu\text{M}$ is the half-saturation constant. Parameters in eqns (6) and (7) were fitted to reproduce the time course of I_{Ca} with and without J_{rel} . Supplemental Fig. S1D shows a measured trace of I_{Ca} just after caffeine application (i.e. depleted SR Ca^{2+}) (dotted grey trace) and for a Ca^{2+} loaded SR (dotted black trace). Comparison of the I_{Ca} traces shows significant acceleration of inactivation and decrease of peak I_{Ca} due to J_{rel} . In addition, a long lasting effect of J_{rel} on the I_{Ca} time course is observed even after 60 ms. These features are well replicated by the I_{Ca} model (see continuous traces in Supplemental Fig. S1D).

Ca_t estimation using J_{rel} modulation of I_{Ca}

Estimation of free Ca^{2+} in the T-space requires formulation of its estimate, $\overline{\text{Ca}}_t$, as a function of J_{rel} -dependent inactivation (RDI) of I_{Ca} . Assuming that J_{rel} is the major Ca^{2+} flux that contributes to Ca_t , the kinetics of I_{Ca} inactivation in the presence of different RDI levels could be used to estimate Ca_t . We assume that RDI is a saturating function of Ca^{2+} , denoted \overline{f}_{Ca} , with a half-saturation constant $K_{\Delta fCa}$. With this assumption, $\overline{\text{Ca}}_t$ is given by:

$$\overline{\text{Ca}}_t = \frac{K_{\Delta fCa}(1 - \overline{f}_{Ca})}{\overline{f}_{Ca}} \quad (8)$$

RDI is a very fast process, with a time constant less than 4 ms (Antoons *et al.* 2007); thus, an instantaneous relation between Ca_t and \overline{f}_{Ca} was assumed. Note that the estimation of Ca_t using eqn (8) does not depend on the protocol used for estimating \overline{f}_{Ca} . To estimate \overline{f}_{Ca} , we utilized the protocol of Acsai *et al.* 2011, shown in Fig. 2. Briefly, after depletion of SR Ca^{2+} with caffeine, the cell was repeatedly stimulated with a voltage pulse of duration 200 ms (i.e. typical AP duration, APD), from a holding potential V_h (-70 mV) to a depolarized potential V_d (10 mV). The magnitude and time course of the resulting I_{Ca} were influenced by VDI and CDI. However, the difference between the first I_{Ca} trace immediately after caffeine application (black trace, denoted I_{Ca}^0) and the following traces of I_{Ca} ($\Delta I_{Ca} = I_{Ca} - I_{Ca}^0$) reflects I_{Ca} inactivation due to J_{rel} only. Note that due to the long (>4 s) interpulse interval, no accumulation of diastolic Ca^{2+} was detected, i.e. the initial phases of Ca_m (<10 ms) were almost identical for all pulses. This implies that most of the Ca^{2+} that entered through LCCs during the 200 ms depolarizing voltage pulses was sequestered by the SR and did not contribute directly to I_{Ca} inactivation. The decline of I_{Ca} was therefore attributed to an augmented J_{rel} due to increased SR Ca^{2+} load with each consecutive pulse. Thus, in forward model simulations (Fig. 2, bottom panels) we generated the data using different (graded) initial values of SR Ca^{2+} content ($\text{Ca}_j = \text{Ca}_n$) to modulate J_{rel} and, in turn, I_{Ca} . Note that zero SR Ca^{2+} content ($\text{Ca}_n = \text{Ca}_j = 0$)

corresponds to experimental conditions after caffeine application. Other Ca_j values were varied from 0.62 to 1.3 mM. As was shown previously (e.g. Shannon *et al.* 2004) and modelled in this study (eqn (A2)), J_{rel} is a steep non-linear function of the SR Ca^{2+} content. Therefore, relatively small changes in Ca_j result in large changes of J_{rel} . The time course of Ca^{2+} in the J-space and N-space is shown in Supplemental Fig. S2.

In the protocol of Fig. 2, any effect due to a small fraction of Ca^{2+} carried via LCCs in the M-space was eliminated by the I_{Ca}^0 subtraction procedure. Because J_{rel} is much larger (10 times; see Fig. 3B) than $J_{Ca,t}$, ΔI_{Ca} is a good surrogate for the time-dependent Ca_t . To convert ΔI_{Ca} into the dimensionless units of \overline{f}_{Ca} , we normalized it by the value of I_{Ca}^0 when ΔI_{Ca} was maximal:

$$\overline{f}_{Ca} = 1 - \frac{\Delta I_{Ca}}{I_{Ca}^0(t_{\Delta \text{max}})} \quad (9)$$

where $I_{Ca}^0(t_{\Delta \text{max}})$ is the value of I_{Ca}^0 at the time ($t_{\Delta \text{max}}$) when the effect of J_{rel} on the I_{Ca} time course is maximal. This normalization procedure eliminates a possible effect of the time onset of J_{rel} on the relative contribution of

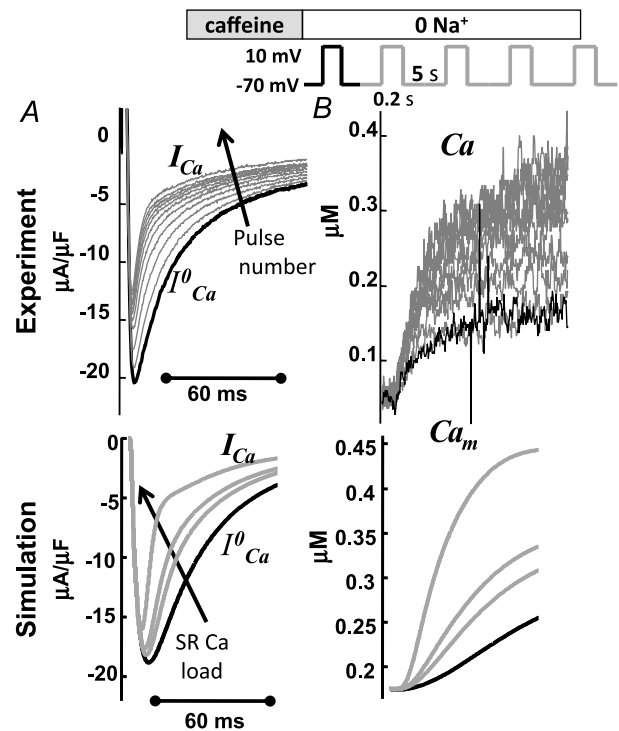


Figure 2. Ca_m and I_{Ca} inactivation increase with increasing SR load

A, superimposed traces of I_{Ca} evoked by depolarizing pulses to 10 mV for 200 ms (inset on top show the experimental protocol). B, corresponding traces of the global Ca^{2+} transient (Ca_m). Experimental recordings are shown at the top, model simulations at the bottom. The first trace of I_{Ca} and of Ca_m after caffeine application (i.e. for depleted SR) is depicted in black. Arrows indicate increasing number of depolarizing pulses.

Ca^{2+} and V to I_{Ca} inactivation. Previously, ΔI_{Ca} was normalized by peak I_{Ca}^0 ; we will discuss the benefits of the new normalization procedure in connection with Fig. 7. It is clear from eqn (8) that in order to accurately estimate $\overline{\text{Ca}}_t$, $K_{\Delta\text{fca}}$ must be known with sufficient accuracy. Values of f_{Ca} affinity to Ca^{2+} (which is largely dependent on calmodulin affinity to Ca^{2+}) were reported in the range 2–10 μM (Saucerman & Bers, 2012); we set the value of $K_{\Delta\text{fca}} = K_{\text{fca}} = 4 \mu\text{M}$.

Ca_t estimation using I_{NCX} and Ca_m : forward and inverse relations between I_{NCX} , Ca_m and Ca_t . Experimental data suggest that I_{NCX} is a saturating function of the intracellular Ca^{2+} concentration, at given values of V and other ion concentrations (Trafford *et al.* 1995; Ottolia *et al.* 2009); it is expressed as follows:

$$I_{\text{NCX}} = \frac{\text{NCX}_{\text{max}}}{1 + K_{\text{ncx}}/\text{Ca}} \quad (10)$$

where the Ca^{2+} -dissociation constant and maximal turnover rate are denoted K_{ncx} and NCX_{max} , respectively. K_{ncx} is estimated to be around 3.6 μM (e.g. Weber *et al.* 2001). This value indicates that NCX responds to Ca^{2+} in T-space dynamically, without saturation. For forward model simulations, NCX_{max} and K_{ncx} in eqn

(10) were determined by best fit to data simulated using eqn (1) in Weber *et al.* 2001 (Supplemental Fig. S3A). NCX_{max} and K_{ncx} depend on V and intracellular sodium concentration (Na_i), respectively. Our simulation shows that K_{ncx} increases from 3 to 11 μM as Na_i increases from 4 to 16 mM (Supplemental Fig. S3B) and is not sensitive to V in the range from -90 to -50 mV. NCX_{max} magnitude decreases from 7.5 to 5 $\mu\text{A} \mu\text{F}^{-1}$ when V increases from -90 to -50 mV (Supplemental Fig. S3C) and is not sensitive to Na_i in the range from 4 to 16 mM.

Unlike the original formulation (Weber *et al.* 2001), eqn (10) can be readily inverted to calculate Ca^{2+} in terms of I_{NCX} , as required for inverse Ca^{2+} estimation. Assuming that total I_{NCX} is the sum of two populations (in T-space and M-space), eqn (10) is represented as follows:

$$I_{\text{NCX}} = \text{NCX}_{\text{max}} \left(\frac{1 - \beta}{1 + K_{\text{ncx}}/\text{Ca}_m} + \frac{\beta}{1 + K_{\text{ncx}}/\text{Ca}_t} \right) \quad (11)$$

where β is the fraction of I_{NCX} in the T-space (sensing Ca_t). Manipulating eqn (11) leads to the following expression

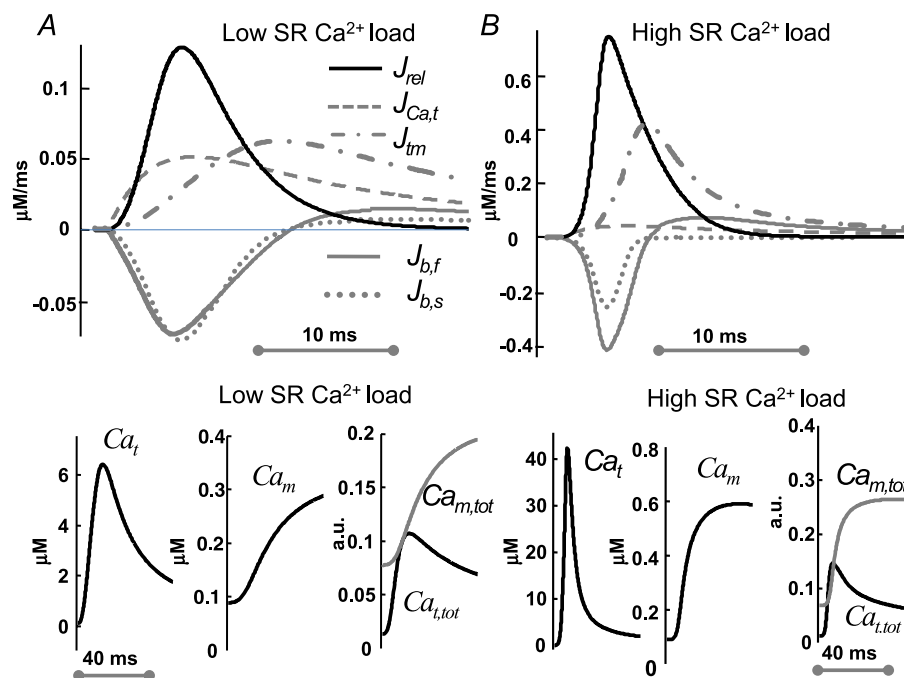


Figure 3. The relative contributions of different Ca^{2+} fluxes to Ca_t is SR-load dependent

The time course of Ca^{2+} fluxes in the T-space (top) and Ca^{2+} redistribution between Ca_t and Ca_m (bottom) as a function of J_{rel} (SR Ca^{2+} load). Top: J_{rel} (black trace), trans-sarcolemmal Ca^{2+} influx, $J_{\text{Ca},t}$ (dashed grey trace), Ca^{2+} efflux from T-space to M-space, J_{tm} (grey dashed-dot trace) and fast ($J_{\text{b},f}$, continuous grey trace) and slow ($J_{\text{b},s}$, dotted grey trace) buffering fluxes. Bottom (left to right): corresponding free Ca_t , free Ca_m and total (free and buffered) Ca^{2+} content in M-space ($\text{Ca}_{m,\text{tot}}$, grey) and T-space ($\text{Ca}_{t,\text{tot}}$, black) as fractions of the total cell Ca^{2+} content. A, at low SR Ca^{2+} load, $\text{Ca}_j = \text{Ca}_i = 0.875$ (small J_{rel}). B, at a large SR Ca^{2+} load, $\text{Ca}_j = \text{Ca}_i = 1.167$ mM (large J_{rel}). Note that panels A and B use different scales and J_{rel} is normalized by v_{jt} (eqn (1)).

for $\overline{Ca_t}$:

$$\overline{Ca_t} = \frac{K_{ncx}}{\beta} \frac{1}{I_{NCX}/NCX_{max} - (1 - \beta)/(1 + K_{ncx}/Ca_m)} - 1 \quad (12)$$

The value of β can be estimated directly using immunohistochemical methods. Here, the parameter β was determined from the best fit of simulated Ca_m and I_{NCX} to those measured experimentally using the caffeine induced J_{rel} protocol. NCX_{max} was calibrated during the phase of Ca_m when both I_{NCX} populations sense the same Ca^{2+} (i.e. $Ca_t = Ca_m$) and eqn (11) reduces to eqn (10). Time to equilibrium of Ca_t with Ca_m was estimated using model simulations.

Ca_t estimation using I_{NCX} and Ca_m : Ca_t estimation using I_{NCX} and Ca_m during J_{rel} induced by a caffeine pulse. A commonly used intervention to study I_{NCX} activity is the caffeine pulse experiment, where rapid application of caffeine depletes the SR Ca^{2+} content and produces a Ca_m rise that activates I_{NCX} (e.g. Trafford *et al.* 1995). We simulated the application of caffeine by increasing the sensitivity of J_{rel} to Ca_t , reducing its refractoriness and decreasing its regulation by SR Ca^{2+} eqn (A2) in Appendix) (Kong *et al.* 2008). In addition, SERCA activity was inhibited (Blinks *et al.* 1972). The time course of caffeine-induced J_{rel} and consequently of Ca_m and I_{NCX} were different from those induced by voltage and I_{Ca} . During caffeine induced J_{rel} , both the J-space and N-space Ca^{2+} pools were depleted. Taking advantage of the fully controlled *in silico* conditions, we utilized a J_{rel} -clamp protocol to simulate caffeine application; the J_{rel} waveform was represented by a Gaussian function, $J_{rel} = A \exp[-(t - \mu)^2/\sigma]$, where the parameters A , μ , and σ were fitted to match the I_{NCX} and Ca_m measured in the experiment, while keeping the total amount of Ca^{2+} released ($\int J_{rel} dt$) constant and equal to the initial total SR Ca^{2+} content.

Ca_t estimation using I_{NCX} and Ca_m : Ca_t estimation using I_{NCX} tail current and Ca_m . We also simulated an I_{NCX} -tail current experiment, which activates J_{rel} by the CICR mechanism via I_{Ca} (Egan *et al.* 1989). Square depolarizing pulses were applied from holding (V_h) to depolarizing (V_d) potentials to ensure cell-wide J_{rel} . The I_{NCX} tail current, measured a few milliseconds after return to V_h , allows for separation of I_{NCX} from all other Na^+ - and Ca^{2+} -dependent currents, which inactivate very rapidly at negative voltages (V_h) and do not contribute significantly to the total current. Optically assessed Ca_m was sampled simultaneously. This procedure was repeated with a progressively increased duration of depolarizing pulses (with increments of Δt ms), which were allowed to

cover the entire duration of the Ca^{2+} transient elicited by J_{rel} . The values of the I_{NCX} and Ca_m were used as input to eqn (12). This method relies on the assumption that J_{rel} is independent of the depolarizing pulse duration.

Results

Relative contributions of Ca^{2+} fluxes to Ca_t are SR-load dependent

Model simulations were conducted to test the assumptions made with regard to contributions of different Ca^{2+} fluxes to the time course of Ca_t . The top panels in Fig. 3 show the time course of Ca^{2+} fluxes in T-space during depolarization to 10 mV for 200 ms, for a small (Fig. 3A) or large (Fig. 3B) J_{rel} (note that J_{rel} in Fig. 3 is normalized by v_{jt} ; eqn (1)). Ca^{2+} contribution to Ca_t from trans-sarcolemmal Ca^{2+} flux into the T-space, $J_{Ca,t}$ (dominated by I_{Ca} , dashed grey) is almost 50% that of J_{rel} (black trace) when J_{rel} is small (due to a small SR Ca^{2+} load, $Ca_j = Ca_n = 0.875$ mM). In contrast, the contribution from $J_{Ca,t}$ is negligible when J_{rel} is large (large SR Ca^{2+} load, $Ca_j = Ca_n = 1.167$ mM). This verifies that J_{rel} is a good surrogate for Ca_t at larger SR Ca^{2+} loads. The time course of Ca^{2+} in the J-space and N-space is shown in Supplemental Fig. S2. Note that small changes in Ca_j result in large changes of J_{rel} . J_{rel} lags slightly behind $J_{Ca,t}$, reflecting the typical CICR sequence. Contributions of the fast ($J_{b,f}$ dotted grey) and slow ($J_{b,s}$ continuous grey) buffers are also J_{rel} dependent. The relative contribution of $J_{b,f}$ increases with increased J_{rel} . Note that initially $J_{b,f}$ and $J_{b,s}$ act as Ca^{2+} sinks (negative fluxes), decreasing Ca_t ; later, the buffering fluxes reverse direction, increasing Ca_t . The buffering fluxes reverse direction earlier (by 5 ms) when J_{rel} is large. The peak of the Ca^{2+} flux from T-space to M-space (J_{tm} , dashed-dot grey curve) coincides with the reversal of the buffering fluxes, demonstrating the importance of including Ca^{2+} buffering sites in the model.

Magnitude and time course of Ca_t and Ca_m are different and SR load dependent

The bottom panels in Fig. 3A show, for small J_{rel} (small SR Ca^{2+} load), Ca_t , Ca_m and the total Ca^{2+} content (free and bound) in M-space ($Ca_{m,tot} = Ca_m + Ca_{trpn} + Ca_{cmdn}$, grey) and T-space ($Ca_{t,tot} = Ca_t + Ca_{b,f} + Ca_{b,s}$, black), normalized by the total cell Ca^{2+} content. Figure 3B shows similar data, but for a large J_{rel} (large SR Ca^{2+} load). Importantly, the results show that even Ca^{2+} flux via I_{Ca} alone has sufficient capacity to increase Ca_t up to ~ 5 μM and thus to induce inactivation of LCCs in T-space. LCCs in M-space are exposed to smaller Ca^{2+} values and

the relative contribution of CDI to their inactivation is smaller.

The time course of $Ca_{m,tot}$ and $Ca_{t,tot}$ indicates that the total amount of Ca^{2+} in the T-space can reach similar values to those in the M-space for a brief period of time, during both small and large J_{rel} , in spite of a large (~ 70 fold) difference in the compartments' volumes. This indicates that buffering capacitance is more important in determining the balance of Ca^{2+} fluxes during dynamic Ca^{2+} transients than the compartmental volumes *per se*.

Partition of NCX between T-space and M-space

To investigate the effect of I_{NCX} localization on Ca_i and to estimate the fraction of NCX in T-space (β), we simulated a caffeine pulse protocol and compared the results to experimental data. The amplitude of the simulated caffeine-induced intracellular calcium transient agrees well with the measurements (compare Fig. 4A right and left panels).

The left panels in Fig. 4 show experimentally recorded Ca^{2+} transient (Ca_m) (Fig. 4A) and I_{NCX} (Fig. 4B) after caffeine induced J_{rel} . A phase plot of I_{NCX} vs. Ca_m is provided in Fig. 4C (same data as in Fig. 4A and Fig. 4B). I_{NCX} is a bi-valued function of Ca_m ; that is, one value of Ca_m (e.g. c_1) is associated with two values of I_{NCX} (α_1 and α_2). Figure 4D shows that I_{NCX} precedes global Ca_m by 25 ms. The right panels in Fig. 4 show the corresponding simulated Ca_m (Fig. 4A) and I_{NCX} (Fig. 4B) as a function of I_{NCX} fractional population in T-space, β (arrow in Fig. 4B indicates increasing β). The corresponding simulated phase plots of I_{NCX} vs. Ca_m are shown in Fig. 4C (right). As in the experiment, I_{NCX} is a bi-valued function of Ca_m ; for example $Ca_m = 0.4 \mu M$ (c_1) is associated with two values of I_{NCX} ($\alpha_1 = -1 \mu A \mu F^{-1}$ and $\alpha_2 = -2.3 \mu A \mu F^{-1}$). Note that for $\beta = 0$ (all I_{NCX} in M-space), I_{NCX} is a single-valued function of Ca_m (dashed grey trace). Thus, the hysteresis and delay between the peaks of Ca_m and I_{NCX} are due to the existence of a population of I_{NCX} that senses Ca_t , which rises faster and reaches higher values than the cell-average Ca^{2+} . The area of the hysteresis loop was

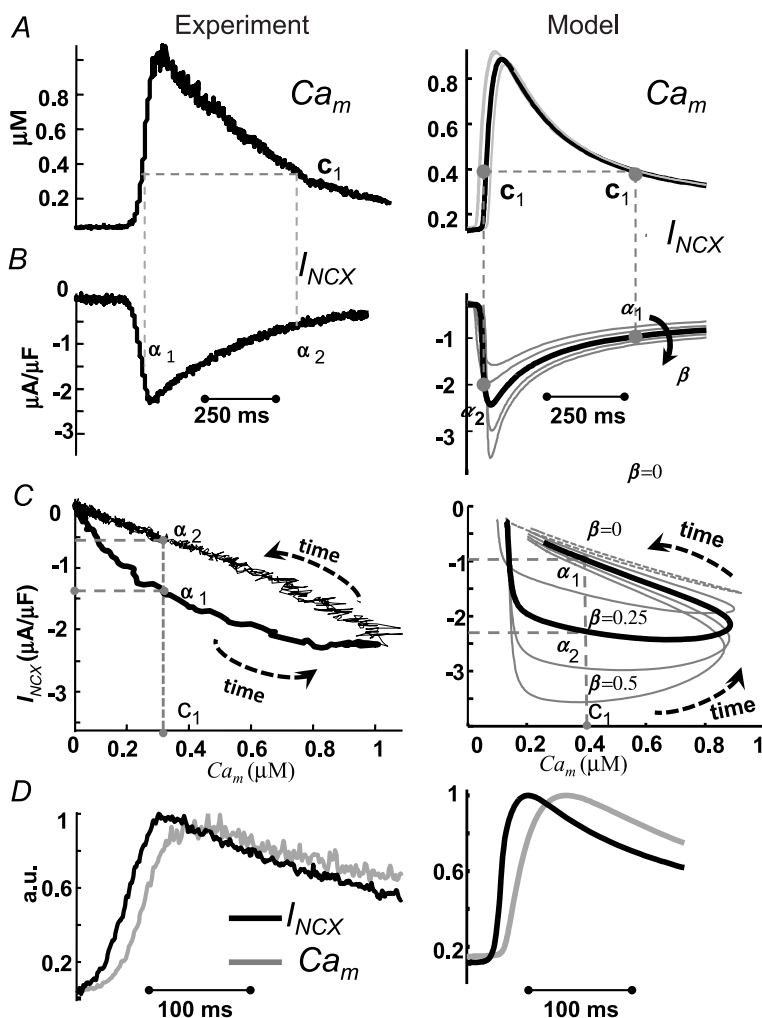


Figure 4. An NCX partition of 25% in T-space and 75% in M-space provides the best fit to experimental data

Peak Ca_m lags by 25 ms relative to peak I_{NCX} , reflecting the NCX partition. The fraction of NCX in T-space, β (right panels), estimated from best fit to experimental data (left panels). Experimentally recorded Ca_m (A, left) and I_{NCX} (B, left) evoked by caffeine pulse; V was held at -80 mV. Phase plots of I_{NCX} vs. Ca_m are constructed in C from the data in A and B. It is clear from panel C that I_{NCX} is a bi-valued function of Ca_m ; that is, one value of Ca_m (e.g. c_1) is associated with two values on I_{NCX} (α_1 and α_2). In panel C, right, β (fraction of NCX in T-space) is varied from 0 to 0.5. The continuous black trace is for 25% of I_{NCX} ($\beta = 0.25$) in the T-space, which provides the best fit for the experimental data. Note that for $\beta = 0$ (grey dashed trace), I_{NCX} is a single-valued function of Ca_m . D, I_{NCX} (black) and Ca_m (grey), corresponding to the traces in panels A and B, are shown on an expanded time scale. Ca_m , normalized to its peak value, is superimposed on normalized and inverted I_{NCX} . Note that peak I_{NCX} precedes peak Ca_m by about 25 ms in both simulation and experiment.

chosen as a criterion for determining the best fit to experimental data; it reflects the difference between the ascending (due to increase of Ca_m) and descending (due to decrease of Ca_m) limbs of the I_{NCX} curves and the relative contribution of Ca_t to whole-cell I_{NCX} . The continuous black curve is for $\beta = 0.25$; it provides the best fit for the experimental data and a similar delay (Fig. 4D) to that measured experimentally. Based on this fit, all estimations of Ca_t were conducted for 25% I_{NCX} in T-space (75% in M-space; $\beta = 0.25$).

Estimation of Ca_t using I_{NCX} and Ca_m due to caffeine induced J_{rel}

Figure 5 shows estimation of Ca_t (\overline{Ca}_t) during a caffeine pulse experiment similar to that in Fig. 4, but from a different cell. V was held constant throughout at -70 mV. The top panels in Fig. 5 show experimentally recorded Ca_m (Fig. 5A) and I_{NCX} (Fig. 5B) after caffeine induced J_{rel} . A phase plot of I_{NCX} vs. Ca_m is provided in Fig. 5C (same data as in Fig. 5A and Fig. 5B). Figure 5D shows measured Ca_m (grey trace) and inverse-estimated \overline{Ca}_t (black trace) using Ca_m and I_{NCX} as input to eqn (12). Na^+ -sensitive

K_{NCX} was set to 3.6 mM and NCX_{max} was estimated to be $11 \mu A \mu F^{-1}$. These results predict a peak Ca_t in the range of $10 \mu M$, with time to equilibrium with global Ca_m of 250 – 350 ms. The Ca_t peak value is an order of magnitude larger than global Ca_m ($1 \mu M$).

The bottom panels of Fig. 5 show model-generated data. As explained in Methods, a J_{rel} -clamp protocol was used (waveform in inset to panel A). The duration of J_{rel} was set so that the time course of Ca_t estimated using experimental data matched that of Ca_t generated by the model. The best fit was achieved with $J_{rel} = 400 \exp[-(t-45)^2/200]$. Model generated Ca_t (black) and Ca_m (dashed grey) are shown in Fig. 5D, bottom; both are very similar to experimental Ca_m and \overline{Ca}_t (Fig. 5D, top). The model predicts that the time course of Ca_m and I_{NCX} during caffeine-pulse experiment is V dependent (Supplemental Fig. S4). Peak Ca_m (Supplemental Fig. S4A) increases and peak I_{NCX} decreases (Supplemental Fig. S4A) with depolarizing voltage. Time to equilibrium between Ca_t and Ca_m shows a moderate V -dependence (Supplemental Fig. S4D); it is shorter for negative V . This is important, because to calibrate NCX_{max} , Ca_m and Ca_t should reach equilibrium.

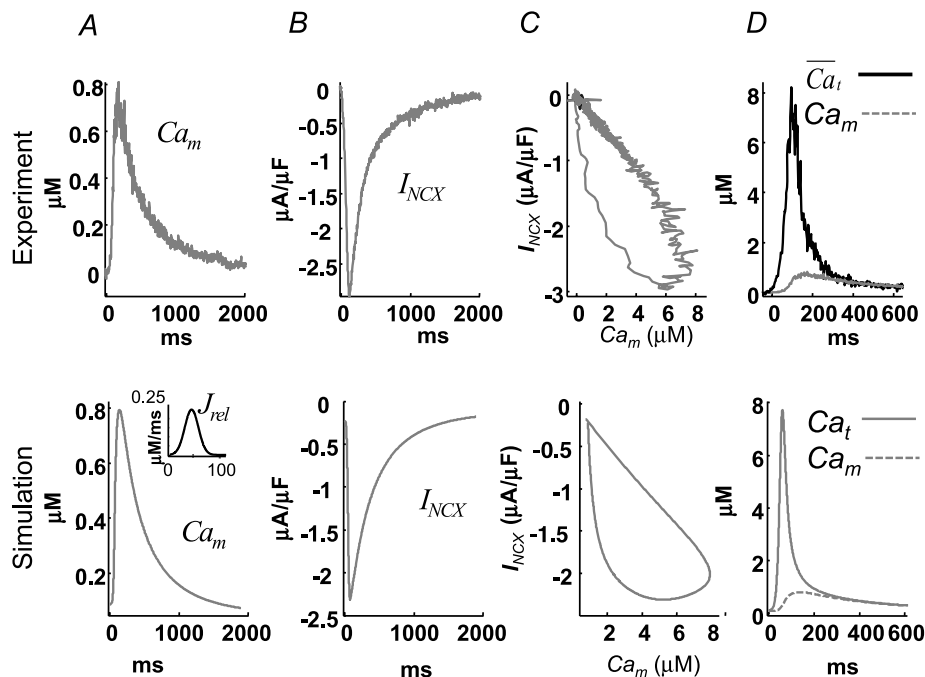


Figure 5. The time course of Ca_t can be estimated from caffeine-induced I_{NCX} and Ca_m ; it shows different dynamics from Ca_t generated by CICR

Experimentally recorded Ca_m (A, top) and I_{NCX} (B, top) evoked by a caffeine pulse; V was held at -70 mV. Phase plots of I_{NCX} vs. Ca_m are constructed in C from the data in A and B. D, estimated Ca_t , \overline{Ca}_t , using eqn (12) with I_{NCX} from A and Ca_m from B as input. For the model-generated data (bottom panels), the J_{rel} waveform shown in the inset to panel A, bottom, was used as input. Model generated (D, bottom) Ca_t (black) and Ca_m (grey) are shown for comparison with those estimated from experimental data (D, top).

Ca_t estimation using *I*_{NCX} tail current and Ca_m due to CICR

Figure 6 shows experimental (top) and simulated (bottom) results of the *I*_{NCX} tail current protocol. During the simulations, similar to experimental protocols, *V* pulses were applied from a holding (−70 mV) to a depolarizing (10 mV) potential. The depolarizing step was interrupted at different time intervals (increments of 10 ms in the experiment), stepping back to −70 mV (see inset in Fig. 6A). In the simulations (bottom panels of Fig. 6), the time increments were decreased to 5 ms in order to increase sampling and thus the quality of the estimation; traces for the first and last *V* pulses are shown as continuous and dashed black lines, respectively. In Fig. 6A changes of *I*_{NCX} tail current amplitude with pulse duration (circles) reflect changes of Ca_t sensed by *I*_{NCX}. Corresponding values of Ca_m were sampled at the same time and are indicated by circles in Fig. 6B; note that the locus of sampled Ca_m values coincides with the Ca_m transient during the last (dashed black) pulse. This indicates that the same *J*_{rel} (and consequently Ca_t) is evoked by each pulse, ensuring that the estimation of \overline{Ca}_t is unique.

Figure 6C shows estimated \overline{Ca}_t from experimental (top) and model generated (bottom) *I*_{NCX} and Ca_m data. In the bottom panel, the actual model-computed Ca_t traces (grey) are also shown as a gold standard for comparison. Importantly, the *I*_{NCX}-based method is able to recover both the ascending and descending limbs of Ca_t. However, it is difficult to estimate the value of peak Ca_t using this method with sufficient accuracy due to the limited number of sampling points, which limits its temporal resolution.

Note that the first three model simulated *I*_{NCX} tail current traces (bottom of Fig. 6A) are biphasic (increasing then decreasing in magnitude) and reach their peaks after the end of the *V* pulse. This non-monotonic behaviour is because Ca_t is still increasing during the first 30 ms of simulation (Fig. 6C). This early phase was not covered by the experimental protocol (top of Fig. 6A). Note that *I*_{NCX} reaches its maximum negative magnitude earlier than peak Ca_m, reflecting the existence of a T-space population of *I*_{NCX} which is activated by Ca_t. Ca_m reaches its peak value at 50 ms, 25 ms later than *I*_{NCX} (arrows in Fig. 6A and B), which corresponds well to the results of the caffeine pulse simulations in Fig. 4D.

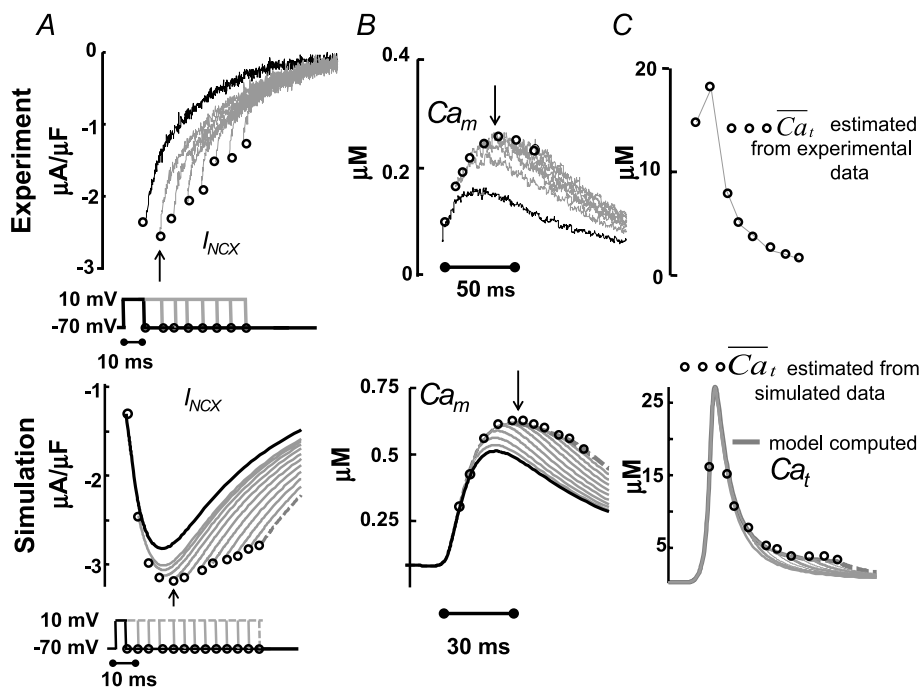


Figure 6. The time course of Ca_t, estimated from the *I*_{NCX} tail current

Estimation of free Ca²⁺ in T-space, \overline{Ca}_t , using experimentally measured (top) and model generated (bottom) *I*_{NCX} and Ca_m, generated by *V* pulses as shown in the inset. A, *I*_{NCX} tail current traces. Raw current traces were truncated before the voltage was returned to the holding potential. Simulated traces, corresponding to the first and last *V* pulses, are shown in continuous and dashed black lines, respectively. B, corresponding optically measured (top) or model simulated (bottom) Ca_m. Circles in panels A and B indicate peaks of *I*_{NCX} tail currents and corresponding Ca_m values. Arrows in A and B indicate peak *I*_{NCX} and Ca_m, respectively. C, estimated Ca_t, \overline{Ca}_t , using eqn (12) with *I*_{NCX} from A and Ca_m from B as input. For the model-generated data (bottom panel), the actual model computed Ca_t is shown (grey traces) together with the estimated \overline{Ca}_t (circles).

Estimation of \overline{Ca}_t using I_{Ca} inactivation as reporter (ΔI_{Ca} -based method)

Model-based validation of the ΔI_{Ca} method. To elucidate the effect of the normalization procedure in eqn (9) on \overline{Ca}_t , we simulated V and Ca_t clamp protocols in Fig. 7. The model cell was depolarized to 10 mV for 200 ms (Fig. 7A top, inset) and Ca_t was also clamped to $20 \mu M$ for 20 ms, with a progressive 5 ms shift of Ca_t pulse onset (Fig. 7A bottom, inset) as indicated by arrow. Figure 7A shows five I_{Ca} traces elicited by the V step, with four Ca_t pulses following the I_{Ca} descending limb. The first I_{Ca} trace (I_{Ca}^0 , blue dashed curve) was simulated without applying a Ca_t pulse, and thus shows inactivation by only a V -dependent mechanism. Figure 7B shows the difference current $\Delta I_{Ca} = I_{Ca} - I_{Ca}^0$; note that peak ΔI_{Ca} is progressively decreased as Ca_t pulses are progressively delayed relative to the V pulse (circles in Fig. 7B). This indicates that the contribution of Ca_t to I_{Ca} inactivation decreases with the delay, despite the identical waveforms of Ca_t pulses. Consequently, calibration of ΔI_{Ca} by peak I_{Ca}^0 results in the \overline{Ca}_t shown in Fig. 7C, which is progressively underestimated as the onset of the Ca_t pulse is increasingly delayed relative to the onset of the V step. This is because I_{Ca} is subjected to V -dependent inactivation immediately after onset of the depolarizing pulse; the longer delay between the V and Ca_t pulses results in greater I_{Ca} inactivation by VDI (not CDI, which is the basis of the ΔI_{Ca} method), smaller ΔI_{Ca} , and consequently a smaller estimate of \overline{Ca}_t . To correct for this artifact of pulse delay, we calibrated each ΔI_{Ca} trace by I_{Ca}^0 values at the time when ΔI_{Ca} was maximal (i.e. contribution of Ca_t to I_{Ca} inactivation was maximal). The resulting \overline{Ca}_t traces are shown in Fig. 7D; note that with this calibration, the peaks

of \overline{Ca}_t are identical (time-invariant), independent of the Ca_t pulse time delay.

Estimation of \overline{Ca}_t from experimental data and comparison to model simulation.

Figure 8 shows estimation of \overline{Ca}_t by the ΔI_{Ca} -based method, using experimental (top panels) and model simulated (bottom panels) data. The experimental data set was from a different cell from the one in Fig. 2; however the V -clamp protocol was identical (inset in Fig. 2). Both experimental and simulated I_{Ca} show similar dependence on J_{rel} . That is, both peak amplitude and residual current decrease as J_{rel} increases. In Fig. 8A the current trace evoked by the first pulse after SR depletion by caffeine is denoted by I_{Ca}^0 (black trace). J_{rel} significantly inactivates and decreases I_{Ca} immediately (~ 2 ms) after J_{rel} initiation, while maximal inactivation of I_{Ca} is reached after 5–10 ms. The model data were generated using graded initial values of $Ca_j = Ca_n$ from 0 to 1.5 mM.

Figure 8B shows the difference current $\Delta I_{Ca} = I_{Ca} - I_{Ca}^0$. The traces exhibit a biphasic behaviour, with a fast initial increase reaching a maximum at around 10 ms, followed by a slow decrease which lasts for more than 60 ms. Model-based analysis of these data clarifies that the first phase of ΔI_{Ca} is dominated by an increase of Ca_t due to J_{rel} , while the second phase is dominated by Ca^{2+} diffusion from T-space to M-space, J_{tm} .

Figure 8C shows estimated f_{Ca} using experimental (top) and simulated (bottom, dashed black) data as input to eqn (9). Circles in Fig. 8A and B indicate I_{Ca}^0 at $t_{\Delta max}$ and maximal ΔI_{Ca} , respectively. Model computed f_{Ca} traces (continuous grey) are shown in Fig. 8C as a gold standard for comparison. The trace of f_{Ca} which corresponds to

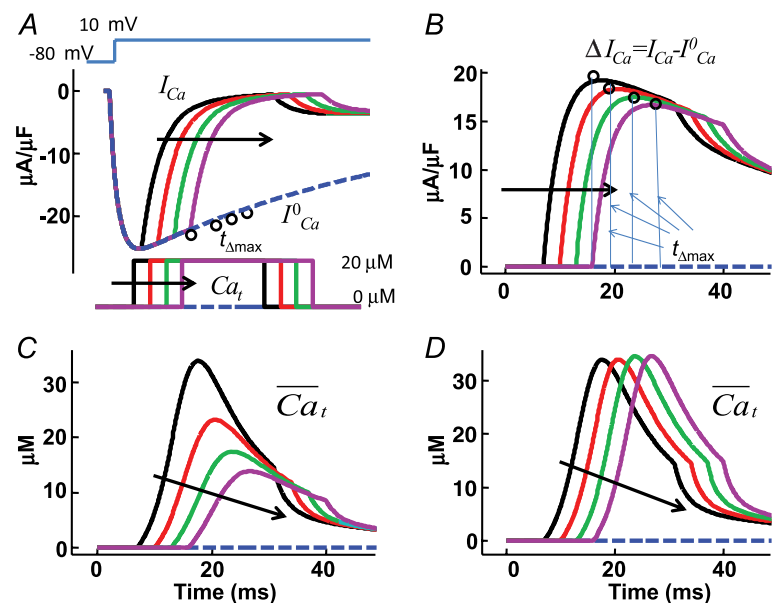


Figure 7. Model-based validation of the ΔI_{Ca} method for estimating Ca_t

A, model simulated traces of I_{Ca} evoked by a depolarizing step to 10 mV (inset on top) in the presence of controlled (calcium clamp) Ca_t pulses of $20 \mu M$ amplitude and 25 ms duration, with progressively delayed onset by 5 ms (arrows; inset on bottom). I_{Ca}^0 , blue dashed trace, is subjected to V -dependent inactivation only (Ca_t set to zero). Circles indicate the values of I_{Ca}^0 at time $t_{\Delta max}$. Note that all traces coincide prior to application of the Ca_t pulse. B, difference current, $\Delta I_{Ca} = I_{Ca} - I_{Ca}^0$. Circles indicate the maximal values of ΔI_{Ca} , occurring at time $t_{\Delta max}$. C, \overline{Ca}_t estimated with ΔI_{Ca} normalized by peak I_{Ca}^0 (old method). D, \overline{Ca}_t estimated by normalizing each ΔI_{Ca} trace by the corresponding value of I_{Ca}^0 at time $t_{\Delta max}$ (eqn (8); new method).

CDI in the absence of RDI ($J_{\text{rel}} = 0$) is denoted by a square symbol. Note that the $\overline{f_{\text{Ca}}}$ trace which corresponds to I_{Ca}^0 (indicated by a star) is equal to unity, i.e. it predicts correctly the absence of I_{Ca} inactivation due to RDI. In contrast, the model computed f_{Ca} trace, indicated by a square, is different from unity. Unlike $\overline{f_{\text{Ca}}}$, which is estimated via RDI (due to J_{rel} only), f_{Ca} accounts for CDI due to all Ca^{2+} fluxes into the T-space. Fluxes other than J_{rel} (via LCC and NCX) contribute to CDI (compare traces indicated by square and star symbols). Clearly, $\overline{f_{\text{Ca}}}$ underestimates CDI of I_{Ca} because it does not consider Ca^{2+} fluxes other than J_{rel} . However, as SR load increases (arrow), J_{rel} increases and the accuracy of $\overline{f_{\text{Ca}}}$ estimation improves, especially during the descending limb of f_{Ca} . Figure 8D shows $\overline{\text{Ca}}_t$ (dashed black traces) estimated using $\overline{f_{\text{Ca}}}$ as an input to eqn (8) (top panel is from experimental data; bottom panel from model generated data). In addition, Fig. 8D (bottom) shows the actual

model computed Ca_t (grey traces) for comparison. Note that the $\overline{\text{Ca}}_t$ trace which corresponds to I_{Ca}^0 (star) is equal to zero (depleted SR, $J_{\text{rel}} = 0$), while the corresponding Ca_t (square) is not (it reaches peak values of 2–3 μM) due to contribution from LCC and reverse-mode NCX. As SR load increases, J_{rel} increases and the accuracy of $\overline{\text{Ca}}_t$ estimation (assessed as the ratio of peak Ca_t to peak $\overline{\text{Ca}}_t$) improves. This is due to an increased contribution of J_{rel} -dependent RDI to total CDI. Using normalized peak differences of the corresponding Ca_t and $\overline{\text{Ca}}_t$ in Fig. 8D (bottom), the estimation error decreases from 47% to 7% as SR load increases.

The ascending phase of Ca_t is estimated with a greater accuracy than the descending phase. This is because the method is based on the J_{rel} component of inactivation and peak J_{rel} coincides with the steepest ascending portion of Ca_t . In addition, a large J_{rel} accelerates inactivation, which makes the instantaneous approximation between Ca_t

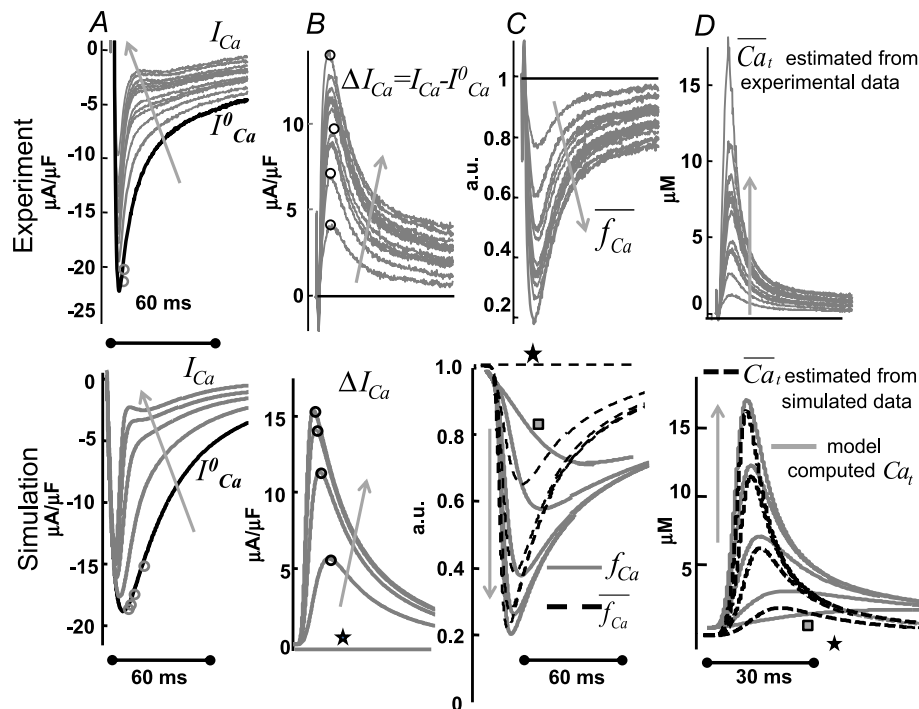


Figure 8. Estimation of Ca_t from J_{rel} -dependent inactivation of I_{Ca} using the ΔI_{Ca} method

Estimation of free Ca^{2+} in T-space ($\overline{\text{Ca}}_t$) using experimentally measured (top) and model simulated (bottom) I_{Ca} . A, superimposed traces of I_{Ca} evoked by depolarizing pulses to 10 mV (V-clamp protocol is identical to that in the inset of Fig. 2); levels of SR Ca^{2+} load increase with the number pulses (arrows). I_{Ca}^0 is the current trace evoked by the first pulse after SR depletion by caffeine (black trace). B, difference current, $\Delta I_{\text{Ca}} = I_{\text{Ca}} - I_{\text{Ca}}^0$; the ΔI_{Ca} trace which corresponds to I_{Ca}^0 (depleted SR; $J_{\text{rel}} = 0$) (continuous black) is equal to zero. Circles indicate the maximal values of ΔI_{Ca} , occurring at time $t_{\Delta \text{max}}$. C, estimate of RDI, $\overline{f_{\text{Ca}}}$. Each ΔI_{Ca} trace was normalized by the I_{Ca}^0 value at the time of maximal ΔI_{Ca} ($t_{\Delta \text{max}}$, indicated by circles in panel A). In the bottom panel, model computed CDI curves, f_{Ca} (grey traces), are also shown for comparison. $\overline{f_{\text{Ca}}}$ and f_{Ca} traces which correspond to I_{Ca}^0 are indicated by a star and a square, respectively. The f_{Ca} trace indicated by a square shows contribution to CDI from Ca^{2+} fluxes other than J_{rel} . D, $\overline{\text{Ca}}_t$ estimated via eqn (8) using $\overline{f_{\text{Ca}}}$ as input. In the bottom panel, model computed Ca_t (grey traces) are also shown for comparison. $\overline{\text{Ca}}_t$ and Ca_t traces which correspond to I_{Ca}^0 are indicated by a star and a square, respectively. The trace indicated by a square shows contribution to Ca_t from Ca^{2+} fluxes other than J_{rel} (via LCC and NCX). Arrows indicate increasing number of depolarizing pulses (SR load).

and inactivation more accurate. However, the I_{Ca} -based method tends to underestimate the descending portion of Ca_t when the relative contribution of J_{rel} to total inactivation is smaller.

Discussion

In this study, we verified that the minimal model for interactions between J_{rel} , I_{Ca} and I_{NCX} requires two myoplasmic functional compartments for Ca^{2+} distribution, T-space and M-space. This compartmental organization differs from the compartmentalization used in previous models (Hund & Rudy, 2004; Shannon *et al.* 2004; Faber *et al.* 2007; Mahajan *et al.* 2008) primarily due to a different partition of LCCs, NCXs and Ca^{2+} buffers. Inclusion of the T-space, which is structurally associated with RyRs, in the compartmental model of Ca^{2+} cycling allowed us to reproduce *in silico* the following important experimental results. (1) Hysteresis of I_{NCX} dependence on Ca_m during a caffeine application protocol (Fig. 4C). (2) A delay between peak I_{NCX} and peak Ca_m during a caffeine application protocol (Fig. 4D). (3) A delay between I_{NCX} and Ca_m during CICR (Fig. 6). (4) A rapid I_{Ca} inactivation (~ 2 ms) due to J_{rel} , with a graded inactivation magnitude as a function of the SR Ca^{2+} content (Fig. 8). (5) A delay between I_{Ca} inactivation due to J_{rel} and due to Ca_m (Fig. 8).

A rapid I_{Ca} inactivation due to J_{rel} indicates a strong functional coupling between LCCs and RyRs in ventricular myocytes, which is not surprising because structurally most of the LCCs and RYRs are located in close proximity to each other. NCXs are usually considered to be expressed outside the Ca^{2+} microdomain of interaction between LCCs and RyRs. However, using the experimental results from the non-failing ventricular myocytes as an input to the compartmental model, we found that a small but significant ($\sim 25\%$) fraction of NCXs is functionally coupled to RyRs via a common pool of Ca^{2+} (Ca_t).

The study provides a theoretical basis for estimating the dynamic properties of Ca_t using measured I_{Ca} , I_{NCX} and Ca_m as input to the compartmental model. The model was used to generate Ca_t transients, simulating specific experimental protocols, and the simulated Ca_t was used as a gold standard for evaluation of inverse-estimated Ca_t using I_{Ca} , Ca_m and I_{NCX} . The simulations confirmed estimations by previous investigators (Egan *et al.* 1989; Trafford *et al.* 1995; Weber *et al.* 2002; Acsai *et al.* 2011), demonstrating that peak Ca_t is an order of magnitude larger than the corresponding peak Ca_m and that Ca^{2+} gradients between T-space and M-space could persist into the late phase of the AP. Previous procedures to estimate Ca_t from Ca^{2+} -dependent currents used a reductionist approach by employing each current in isolation. Here we

used data from both I_{Ca} and I_{NCX} , where J_{rel} was induced by either CICR or by caffeine application. The results revealed that the I_{Ca} -based method is more accurate during the rising phase of Ca_t , while the I_{NCX} -based method is more accurate during its slow descending phase. Combined application of both methods provides a close estimate of both phases and a more accurate estimate of the entire Ca_t than the application of each method alone.

Characteristics of free Ca^{2+} in T-space (Ca_t)

The model predicts peak Ca_t in the range of 6–25 μM ; these values are similar to computed Ca^{2+} transients averaged over many dyadic spaces (15 μM , Bondarenko *et al.* 2004; Greenstein *et al.* 2006), but significantly lower than the maximal values computed for a single dyad (> 50 μM , Stern, 1992; Langer & Peskoff, 1998; Higgins *et al.* 2007; Gaur & Rudy, 2011). These results are consistent with our definition of T-space, which assumes a uniform whole-cell J_{rel} and an average Ca_t over many dyads. We also found that the time to equilibrium between Ca_t and Ca_m was strongly dependent on the experimental conditions, including the amount of Ca^{2+} released via RyRs (SR Ca^{2+} load) and the magnitude of the depolarizing V pulses (the driving force for I_{NCX}) (Supplemental Fig. S4). An increase of J_{rel} and/or of V increased the time to equilibrium, which was in the range of 50–350 ms, depending on J_{rel} and V . The lower bound of these values are consistent with those previously computed in models for CICR (Shannon *et al.* 2004; Greenstein *et al.* 2006; Faber *et al.* 2007). The caffeine pulse protocol shows significant prolongation of Ca_t duration (Fig. 5).

We found that the time course of Ca_t is strongly regulated by fast and slow Ca^{2+} buffers (Fig. 3). We also found that J_{rel} significantly inactivates and decreases I_{Ca} immediately (~ 2 ms) after J_{rel} initiation, while maximal inactivation of I_{Ca} due to J_{rel} is reached after 5–10 ms.

The compartmental model of Ca^{2+} cycling

The success of inverse Ca_t estimation depends on the accuracy of the mathematical model used, and how well constrained is the model by experimental data. The model should describe quantitatively the relationship between the time course of Ca^{2+} -dependent currents and the time course of Ca^{2+} which modulates them. Below we discuss modelling considerations for I_{Ca} and I_{NCX} .

Accuracy of the I_{Ca} model. In the I_{Ca} model development, we utilized experimental data from porcine ventricular myocytes. Using the Hodgkin–Huxley formalism, model activation and inactivation gates were fitted to reproduce the recorded I_{Ca} I – V curve (Supplemental Fig. S1). Note that the I – V curve is SR Ca^{2+} load dependent (Sham,

1997). I_{Ca} inactivation was assessed by the conventional two-step voltage-clamp protocol (Stengl *et al.* 2010) (Supplemental Fig. S1). Following (Kass & Sanguinetti, 1984; Lee *et al.* 1985; Hadley & Hume, 1987) we assumed that I_{Ca} inactivation is V dependent and is not complete in the absence of Ca^{2+} . In the model, I_{Ca} inactivation was characterized by the product of two time-dependent processes: (1) voltage-dependent inactivation modulated by Ca^{2+} , and (2) a pure free Ca^{2+} -dependent process. Ca^{2+} -dependent parameters were fitted to reproduce the magnitude and time course of I_{Ca} and its dependence on J_{rel} (variable SR Ca^{2+} load) (Fig. 2). To validate the model in the context of whole cell Ca^{2+} cycling, we verified that it reproduces experimentally recorded whole cell Ca^{2+} transients and I_{Ca} at different levels of SR Ca^{2+} load. Model simulated results match simultaneously the experimentally recorded I_{Ca} (Fig. 2A) and Ca_m (Fig. 2B) at different levels of J_{rel} (SR Ca^{2+} load).

Accuracy of the I_{NCX} model. Bidirectional flux of Ca^{2+} through NCX depends on V , intracellular concentration (Na_i) and extracellular concentration (Na_o) of Na^+ and extracellular concentration of Ca^{2+} (Ca_o), which complicates the analysis. To keep I_{NCX} operating in the forward (Ca^{2+} extrusion) mode, experimental protocols were conducted at constant V close to the resting values (~ -80 mV) and at low Na_i (< 5 mM). Since Na_o and Ca_o can be controlled in experiments, measured I_{NCX} can be regarded as a function of Ca_m and Ca_t only. An independent measurement of Ca_m (whole-cell optical signal) allows for a unique estimate of Ca_t . The formulation proposed by Weber *et al.* (2001) was used as a starting point for I_{NCX} modelling here. The slow allosteric dependence of I_{NCX} on intracellular Ca^{2+} was eliminated based on the recent study of Reeves & Condrescu (2003). We show that the resulting I_{NCX} model (eqn (10)) can be approximated by a Hill equation with a variable intracellular Ca^{2+} at fixed Na_o , Ca_o , Na_i and V , conditions that can be realized experimentally. This formulation (eqn (10)) was inverted to calculate Ca_t in terms of I_{NCX} , as required for inverse $\overline{Ca_t}$ estimation (eqn (12)).

Spatial constraints

In ventricular myocytes, Ca^{2+} concentration gradients exist between SR dyads, a subsarcolemmal space (including caveolae) and the bulk myoplasm (Trafford *et al.* 1995; Weber *et al.* 2002; Higgins *et al.* 2007). The model used here does not consider the dynamics of Ca^{2+} in individual dyadic spaces (Shannon *et al.* 2004; Gaur & Rudy, 2011); instead all dyads are incorporated into the T-space and their Ca^{2+} concentration is assumed to be in rapid equilibrium. This implies that no Ca^{2+} gradients exist between dyads. Consistently, the experimental

protocols evaluated here rely on the cell-average Ca^{2+} and are not designed to estimate Ca^{2+} in a single dyad. Therefore, we implemented protocols for which RyRs are activated uniformly throughout the cell, either by CICR (via LCC flux) or by caffeine-induced- Ca^{2+} release.

The physical characteristics of T-space

Unlike structurally defined, membrane delimited organelles such as the myoplasm, sarcoplasmic reticulum, nucleus, or mitochondrion, subsarcolemmal compartments have been considered as functional, with little correspondence to the actual structural organization of the cell (e.g. Standen & Stanfield, 1982; Shiferaw *et al.* 2003; Shannon *et al.* 2004). Here, T-space and M-space are functional compartments; however, their physical characteristics, i.e. size, localization of Ca^{2+} sensitive proteins (LCC, NCX, RyR), buffers, and Ca^{2+} fluxes into and out of the compartments were determined based on the structural organization of the porcine ventricular myocyte and using best fit to experimental data. T-space is enclosed by the T-tubules portion of the sarcolemma and the junctional portion of the SR membrane. M-space is enclosed by the non-tubular sarcolemma and the non-junctional SR membrane. LCCs and NCXs reside with different densities in the sarcolemma of T-space and M-space. Note (Fig. 1A) that a portion of the T-tubular membrane can be outside the T-space and LCCs and NCXs there sense M-space Ca^{2+} .

The effects of the spatial localization of I_{NCX} on Ca_m were investigated with a simulated caffeine induced J_{rel} (Fig. 4). Experiments show that the time course of global Ca^{2+} lags (> 30 ms) behind I_{NCX} . Interpretation of this result is not unique and is model dependent. For example, Weber *et al.* (2002) and Trafford *et al.* (1995) showed that the existence of a single diffusion barrier between the subsarcolemmal space (where all I_{NCX} were located in their models) and the bulk myoplasm is sufficient to account for this phenomenon; the time constant of Ca^{2+} diffusion flux between the subsarcolemmal space and global myoplasm was used as a fitted parameter in these studies. We used a different approach in this study; instead of fitting the time constant of J_{tm} , we used the fraction of I_{NCX} in the T-space, β , as a parameter. Best fit to the experimental data was obtained for 25% of I_{NCX} in the T-space, 75% of I_{NCX} in the M-space.

The quantity of sarcolemmal and SR membrane anionic Ca^{2+} binding sites ('buffers') in the T-space defines the functional 'size' of this compartment. Note that, the effective buffering capacity depends strongly on the kinetics of the buffers (dissociation constants) and not only on the number of available binding sites *per se*. This effective size depends on the membrane surface area that encloses this compartment (which is large) and not on

the myoplasmic volume that it encloses (which is small). The effective size of the T-space compartment depends on the Ca^{2+} sensitivity (half-saturation constants) of J_{rel} , I_{Ca} and I_{NCX} ; it is estimated to be in the range of 0.5–10 μM (units of concentration; Hofer *et al.* 1997; Bers, 2001; Ottolia *et al.* 2009). An increase of sensitivity (i.e. a decrease of half-saturation constants) will increase the effective size of the T-space. In fact the T-space merges with the M-space when the half-saturation constants drop below the average Ca_m . A similar merger occurs if J_{tm} is large and time to equilibrium between Ca_t and Ca_m is short.

The use of I_{NCX} and I_{Ca} as Ca^{2+} sensors requires that their sensitivity to Ca^{2+} (half-saturation constants, K_d) is in the range of expected values of the local Ca^{2+} concentration. If the local Ca^{2+} concentration is too low ($\ll K_d$) its ability to affect these currents is blunted. Similarly, if it is too high ($\gg K_d$) the dependence of these currents on Ca^{2+} reaches saturation and sensitivity is lost.

Number of compartments in the model. The representation of the structure in Fig. 1A by the compartmental model in Fig. 1B is not unique. Obviously, during the transition from a 3D structure to a compartmental model certain assumptions must be made. Several studies used three-compartment myoplasmic models (dyads, subsarcolemmal space and bulk myoplasm) or two-compartment models (subsarcolemmal space and bulk myoplasm). Inter-compartmental fluxes and partition of major Ca^{2+} -sensitive proteins vary greatly between models. We assumed that regardless of the number of compartments in the model, the total amount of Ca^{2+} and total trans-sarcolemmal Ca^{2+} flux should be conserved. This conservation relation greatly decreases the parameter space of the model (Livshitz & Rudy, 2009). The strategy to include only two Ca^{2+} myoplasmic subcompartments was motivated by the need to ensure that the model is tractable and its parameters are experimentally verifiable. Importantly, it allowed us to formulate an analytic inverse relation between the Ca^{2+} -dependent currents (I_{Ca} and I_{NCX}) and Ca_t .

Evaluation of methods for estimating Ca_t

We evaluated the validity of the experimental methods for Ca_t estimation by simulating the experimental protocols and comparing the inverse-estimated $\overline{\text{Ca}_t}$ with the model-computed Ca_t . The results show that under ideal and fully controlled *in silico* conditions, all methods that use a V -clamp protocol to activate J_{rel} result in similar estimates of Ca_t , providing that the SR Ca^{2+} load and the depolarizing pulses are the same. Not surprisingly, the amplitude and duration of Ca_t induced by

caffeine varies greatly from that induced by depolarization (compare Figs 4–5 and 7–8). Typically, Ca_t induced by caffeine has a significantly longer duration than its depolarization-induced counterpart.

Estimation of Ca_t using tail I_{NCX} current and Ca_m . We show (Fig. 6) that estimation of Ca_t using the I_{NCX} -based method provides a good estimate for the descending phase of Ca_t . This method is less sensitive to the SR Ca^{2+} load than the I_{Ca} -based method, as it does not require modulation of the SR Ca^{2+} load. The quality of the estimation increases when the number of sampling points increases (duration of testing pulses decreases), a condition that can be difficult to achieve in experiments. An advantage of the I_{NCX} -based method is that pharmacological interventions are not required. However, in this method a greater number of parameters must be fitted. Parameter sensitivity analysis indicates that the accuracy is strongly dependent on the specified fraction of I_{NCX} in the T-space. In addition, the model used for the estimation should be re-calibrated for each set of ion concentrations (Na_o , Ca_o , Na_i) and test potential V .

Estimation of Ca_t using I_{Ca} . To derive an analytical expression for Ca_t as a function of I_{Ca} , several assumptions were made. Since J_{rel} provides the dominant contribution to Ca_t in ventricular myocytes, its contribution to I_{Ca} inactivation (denoted RDI) was used as a surrogate for Ca_t (Sham, 1997). To isolate the J_{rel} -dependent component from I_{Ca} traces, the I_{Ca} trace in the absence of J_{rel} (I_{Ca}^0) was subtracted from those in the presence of J_{rel} (Acsai *et al.* 2011). The ΔI_{Ca} -based method does not depend on the partition of LCCs between the T-space and M-space, because the effects of M-space LCCs is eliminated by the subtraction procedure. We formulated the Ca^{2+} -dependent inactivation of I_{Ca} as a function of free Ca^{2+} concentration assuming that the contributions of Ca^{2+} fluxes to changes in the Ca^{2+} concentration are additive (eqn (1)). To convert the resulting difference current, ΔI_{Ca} ($\mu\text{A } \mu\text{F}^{-1}$), into the dimensionless units of Ca^{2+} -dependent inactivation, f_{Ca} , we calibrated ΔI_{Ca} by the value of I_{Ca}^0 at the time when ΔI_{Ca} reached its maximum (i.e. contribution of Ca_t to I_{Ca} inactivation was maximal, Fig. 7B). Taking advantage of the completely controlled *in silico* conditions, we simulated a double (V and Ca^{2+}) clamp protocol (Fig. 7) to study the effect of the delay between depolarization (V step) and CICR (Ca^{2+} pulse) on the relative dynamics of VDI and CDI of I_{Ca} . We found that an increased delay between the onset of the V step and the Ca^{2+} step (which can happen under pathophysiological condition that impair J_{rel} ; Bito *et al.* 2008) reduced the relative contribution of CDI to total I_{Ca} inactivation, even

when the Ca^{2+} pulse shape and duration were held constant. Thus, calibrating ΔI_{Ca} by peak I_{Ca}^0 (eqn (9)) and using the resulting \bar{f}_{Ca} as an input to eqn (8) underestimates Ca_t . The proposed new calibration procedure does not suffer from this artifact (compare Fig. 7C and D).

The method presented here is based on steady state (time-independent) approximations of Ca^{2+} -dependent inactivation of I_{Ca} and Ca^{2+} -dependent activation of I_{NCX} . It was shown that inactivation of I_{Ca} induced by J_{rel} is a fast process (e.g. Antoons *et al.* 2007; Puglisi *et al.* 1999), especially at high SR Ca^{2+} loads (i.e. large J_{rel} and Ca_t) and therefore this assumption is well justified. The steady-state approximation allowed us to use an analytic expression for Ca_t as a function of f_{Ca} . During a voltage pulse, the inverse estimation of Ca_t using the ΔI_{Ca} -based method provided the best accuracy at high SR Ca^{2+} load, when I_{Ca} is sufficiently small relative to J_{rel} and does not contribute substantially to Ca_t , i.e. when the gain of CICR (i.e. $J_{\text{rel}}/J_{\text{Ca,t}}$ ratio) is high, which is true under normal physiological conditions.

With the I_{Ca} -based method, the ascending phase of Ca_t is estimated with a greater accuracy than the descending phase (Fig. 8D) (the opposite is true for the I_{NCX} -based method). This is an expected result, because this method is based on the J_{rel} -component of inactivation and peak J_{rel} coincides with the steepest ascending portion of Ca_t . However, during the descending portion of Ca_t the contribution of J_{rel} to inactivation is decreased, resulting in a less accurate estimate. Therefore, combination of the I_{Ca} and I_{NCX} -based methods provides an estimate for the entire Ca_t time course.

New insights and potential future applications of the model

Beyond estimation of Ca_t , the compartmental model presented here provides a conceptual framework for studying the interactions between dynamic Ca^{2+} , I_{Ca} and I_{NCX} in the functional microdomain where they interact physiologically (T-space). The functional compartmentalization is different from that in previous models; it does not employ a uniform subsarcolemmal 'subspace', but a functional volume near RyR (Acsai *et al.* 2011), where subpopulations of I_{Ca} and I_{NCX} (estimated here at 90% I_{Ca} and 25% I_{NCX}) interact with RyR through a common Ca^{2+} pool. The compartmentalization and partition are based on an interpretation of experimental data obtained under voltage clamp conditions and controlled SR Ca^{2+} load. For this compartmentalization, we estimated a peak Ca_t in the range of 6–25 μM , with time to equilibrium between Ca_t and Ca_m of about 350 ms. The Ca_t values are in the range of LCC and RyR sensitivity to Ca^{2+} , which implies that there is a

significant effect of Ca^{2+} in this domain on their kinetics and, in turn, on the action potential during physiological cell excitation. A natural continuation of the work presented here will be an implementation and application of the model to study cellular excitation and Ca^{2+} cycling under physiological conditions (i.e. an expansion from the controlled, clamped protocols implemented here) and during disease states associated with various pathologies.

Appendix

Units and equations

Physical units are as in the original LRd paper (Luo & Rudy, 1994): time (t) in milliseconds (ms), membrane voltage (V) in millivolts (mV), current through channel X (I_X) in microamperes per cell capacitance ($\mu\text{A } \mu\text{F}^{-1}$), channel conductance (G_X) and maximal channel conductance (\bar{G}_X) in millisiemens per microfarad ($\text{mS } \mu\text{F}^{-1}$), intracellular and extracellular ion concentrations (X_i , X_o) in millimoles per liter (mM). Inter-compartmental Ca^{2+} fluxes are defined in terms of millimoles per liter (of the compartment indicated by the first subscript) per millisecond (mM ms^{-1}). Gating variables are given by their steady state and time constant expressions x_∞ and τ_x (ms), or by forward α_x and backward β_x rate constants (ms^{-1}) as follows: $dx/dt = (x_\infty - x)/\tau_x = \alpha_x(1 - x) - \beta_x x$. Model equations and computer code can be found in the research section of <http://rudylab.wustl.edu>. The notations $\varphi = F/R/T = 0.0374 \text{ (V}^{-1}\text{)}$ and $\psi = V\varphi$ are used in equations, where $R = 8314 \text{ (J mol}^{-1}\text{ K}^{-1}\text{)}$ is the universal gas constant, $F = 96,485$ is the Faraday constant (C mol^{-1}) and $T = 310$ is the absolute temperature (K); $z_{\text{Ca}} = 2$ is the valence of Ca^{2+} ions.

Geometrical considerations

Following the LRd model structure (Luo & Rudy, 1994), the M-space volume was set to $v_m = 25 \times 10^{-6} \mu\text{l}$, leaving 30% of the total cell volume ($v_{\text{cell}} = 38\text{e-}6 \mu\text{l}$) inaccessible to ions due to the presence of mitochondria and other organelles. The SR volume (6% of v_{cell}) was subdivided into J-space ($v_j = 0.138\text{e-}6 \mu\text{l}$) and N-space ($v_n = 2.1 \times 10^{-6} \mu\text{l}$), v_t was set conservatively to $0.38 \times 10^{-6} \mu\text{l}$, 1% of v_{cell} . To ensure Ca^{2+} conservation, any change in a compartment volume should be accompanied by a change in the total Ca^{2+} concentration. Thus, a decrease of v_t should be accompanied by a corresponding increase in concentration of Ca^{2+} binding sites (buffers) to preserve the total amount of cell Ca^{2+} .

Due to cell size variability, experimental recordings of I_{Ca} and I_{NCX} ($\mu\text{A } \mu\text{F}^{-1}$) were normalized by the total cell capacitance C_{cell} (μF), which varied from 0.09 to 0.2 μF .

Table 2. Ca²⁺ buffers (Bers, 2001)

Name of buffer	$k_d = k_-/k_+$ (mM)	k_- (1/ms)	k_+ (1/mM ms ⁻¹)	\bar{X} Maximal concentration (mM)
M-space troponin	0.5e-3	0.02	40	50e-3
M-space calmodulin	2.4e-3	0.24	100	70e-3
T-space fast	0.5e-3	0.05	100	0.7
T-space slow	10e-3	0.1	100	1.32
J-space calsequestrin	0.8	80	100	10

To convert Ca²⁺ currents into units of Ca²⁺ fluxes, an average value of $C_{cell} = 0.15 \mu F$ was assumed, which is very close to the value used in LRd (0.1534 μF). Note that the capacitive areas of the T-tubular and non-tubular portions of the sarcolemma are assumed equal $C_m = C_t = 0.075 \mu F$. Extracellular ion concentrations were set to the values in corresponding experiments.

Ca²⁺ buffering fluxes

The Ca²⁺ flux to and from a buffer protein X ($J_{b,x}$) is formulated as a first order kinetic equation:

$$J_{b,x} = \frac{dCa_x}{dt} = k_x^+(\bar{X} - Ca_x) \cdot Ca_y - k_x^- Ca_x \quad (A1)$$

where Ca_x is bound Ca²⁺ to buffer x ; Ca_y is free Ca²⁺ in compartment y . The buffering fluxes in M-space ($J_{bf,m}$) include binding–unbinding to troponin and calmodulin Ca²⁺ binding sites. The buffering flux in T-space involves fast and slow components ($J_{bf,t} = J_{b,f} + J_{b,s}$). These are composed of sarcolemmal anionic binding sites (Post & Langer, 1992), and Ca²⁺/calmodulin binding sites to LCC, RyR and CaMKII (Saucerman & Bers, 2012). Kinetics of the fast and slow buffers were adjusted to best fit I_{Ca} inactivation. Volumes of functional Ca²⁺ compartments, their buffering capacity, and Ca²⁺ fluxes between compartments are interdependent. Therefore, conservation of total cell Ca²⁺ was imposed as an additional constraint. Calsequestrin (J_{csqn}) is located in J-space. Forward (k_x^+) and backward k_x^- rate constants and total concentration (\bar{X}) of protein X binding sites are summarized in Table 2.

Ca²⁺ flux from J-space to T-space (J_{jt})

J_{jt} has two components, J_{rel} and J_{leak} . J_{leak} is an intrinsic RyR Ca²⁺ leak, which depends on the Ca²⁺ gradient: $J_{leak} = k_{leak}(Ca_j - Ca_t)$. The J_{rel} model is based on a previously published model (Livshitz & Rudy, 2007). Following Faber & Rudy (2000), J_{rel} is activated by the flux of free Ca²⁺ into the T-space, regardless of its origin (J_{Ca} , J_{NCX} , J_{tm}). In addition, to simulate caffeine-induced J_{rel} , we included luminal (SR) activation of RyR in the

model. The differential equation that describes J_{rel} is of the form:

$$dJ_{rel}/dt = (J_{rel,\infty} - J_{rel})/\tau_{rel} \quad (A2)$$

$J_{rel,\infty} = \alpha_{rel}(A_{rel} + B_{rel})D_{rel}$ represents the steady-state value of J_{rel} ; $\tau_{rel} = \beta_{\tau}/(1 + K_{rel,\tau}/Ca_j)$ is the time constant, $K_{rel,\tau} = 0.0123$, $\beta_{\tau} = 4.75$ is the maximal value of τ_{rel} , $\alpha_{rel} = 12 \beta_{\tau}$ is the amplitude coefficient. $J_{rel,\infty}$ is expressed as a product of the sum of cytosolic (A_{rel}) and luminal (B_{rel}) Ca²⁺-dependent activation with luminal deactivation (D_{rel}). $A_{rel} = dCa_t/dt$ when dCa_t/dt is positive, and $A_{rel} = 0$ otherwise. Similarly, B_{rel} is not zero only above a certain level of Ca_j (threshold). This formulation involves logical expressions that introduce singularities which can cause problems for implementation in a problem solving environment such as MATLAB and for numerical analysis. To remove singularity, we follow the method in Livshitz & Rudy (2009) and introduce an auxiliary function $\lambda(x) = 1/[1 + \exp(-x\gamma)]$, where γ is a small (e.g. 1×10^{-8}) number. $\lambda(x)$ is equal to unity for a positive argument and zero otherwise. Formulations of A_{rel} and B_{rel} in terms of $\lambda(x)$ are $A_{rel} = (dCa_t/dt) \cdot \lambda(dCa_t/dt)$ and $B_{rel} = \lambda(\text{Threshold} - Ca_j)$. Ca_j -dependent deactivation was modelled as a steep saturating function of Ca_j : $D_{rel} = 1/[1 + (K_{rel,\infty}/Ca_j)^h]$, where $K_{rel,\infty} = 1 \text{ mM}$ is the half-saturation coefficient and $h = 9$. Application of caffeine was simulated by a gradual decrease of $K_{rel,\infty}$ to zero, and by simultaneous increase of α_{rel} and k_{leak} .

J_{mn} (bidirectional) flux between the M-space and the N-space

J_{mn} is described by a phenomenological equation, as proposed in Shannon *et al.* (2004)

$$J_{mn} = \bar{J}_{SERCA} \frac{(Ca_m/K_{up})^h - (Ca_n/nSR)^h}{1 + (Ca_m/K_{up})^h + (Ca_n/nSR)^h} - k_{leak}(Ca_n - Ca_m) \quad (A3)$$

nSR (maximal affinity to SR Ca) = 15 mM, $\bar{J}_{SERCA} = 0.875 \times 10^{-3} \text{ mM ms}^{-1}$, $K_{up} = 0.8 \times 10^{-3} \text{ mM}$, $h = 1.7$.

References

- Adachi-Akahane S, Cleemann L & Morad M (1996). Cross-signaling between L-type Ca^{2+} channels and ryanodine receptors in rat ventricular myocytes. *J Gen Physiol* **108**, 435–454.
- Adler D, Wong AY & Mahler Y (1985). Model of mechanical alternans in the mammalian myocardium. *J Theor Biol* **117**, 563–577.
- Adrian RH (1983). Electrical properties of striated muscle. In *Handbook of Physiology*, section 10, *Skeletal Muscle*, ed. Peachy L, pp. 275–300. American Physiological Society, Bethesda, MD.
- Acsai K, Antoons G, Livshitz L, Rudy Y & Sipido KR (2011). Assessment of $[\text{Ca}^{2+}]$ near ryanodine receptors during sarcoplasmic reticulum Ca^{2+} release with L-type Ca^{2+} and Na/Ca exchange currents as $[\text{Ca}^{2+}]$ reporter. *J Physiol* **589**, 2569–2583.
- Allbritton NL, Meyer T & Stryer L (1992). Range of messenger action of calcium ion and inositol 1,4,5-trisphosphate. *Science* **258**, 1812–1815.
- Antoons G, Volders PGA, Stankovicova T, Bito V, Stengl M, Vos MA & Sipido KR (2007). Window Ca^{2+} current and its modulation by Ca^{2+} release in hypertrophied cardiac myocytes from dogs with chronic atrioventricular block. *J Physiol* **579**, 147–160.
- Atkins GL (1969). *Multicompartment Models for Biological Systems*. Methuen & Co. Ltd., London.
- Belevych AE, Terentyev D, Terentyeva R, Nishijima Y, Sridhar A, Hamlin RL, Carnes CA & Györke S (2011). The relationship between arrhythmogenesis and impaired contractility in heart failure: role of altered ryanodine receptor function. *Cardiovasc Res* **90**, 493–502.
- Bers DM (2001). *Excitation–Contraction Coupling and Cardiac Contractile Force*. Kluwer Academic Publishers, Dordrecht.
- Bito V, Heinzel FR, Biesmans L, Antoons G & Sipido KR (2008). Crosstalk between L-type Ca^{2+} channels and the sarcoplasmic reticulum: alterations during cardiac remodeling. *Cardiovasc Res* **77**, 315–324.
- Blinks JR, Olson CB, Jewell BR & Braveny P (1972). Influence of caffeine and other methylxanthines on mechanical properties of isolated mammalian heart muscle. *Circ Res* **30**, 367–392.
- Bootman MD, Higazi DR, Coombes S & Roderick HL (2006). Calcium signalling during excitation-contraction coupling in mammalian atrial myocytes. *J Cell Sci* **119**, 3915–3925.
- Bondarenko VE, Sziget G, Bett GCL, Kim S-J & Rasmusson RL (2004). Computer model of action potential of mouse ventricular myocytes. *Am J Physiol Heart Circ Physiol* **287**, H1378–H1403.
- Chen-Izu Y, McCulle SL, Ward CW, Soeller C, Allen BM, Rabang C, Cannell MB, Balke CW & Izu LT (2006). Three dimensional distribution of ryanodine receptor clusters in cardiac myocytes. *Biophys J* **91**, 1–13.
- Drummond GB (2009). Reporting ethical matters in *The Journal of Physiology*: standards and advice. *J Physiol* **587**, 713–719.
- Egan TM, Noble D, Noble SJ, Powell T, Spindler AJ & Twist VW (1989). Sodium-calcium exchange during the action potential in guinea-pig ventricular cells. *J Physiol* **411**, 639–661.
- Faber GM, Silva J, Livshitz L & Rudy Y (2007). Kinetic properties of the cardiac L-type Ca channel and its role in myocyte electrophysiology: A theoretical investigation. *Biophys J* **92**, 1522–1543.
- Faber GM & Rudy Y (2000). Action potential and contractility changes in $[\text{Na}^+]_i$ overloaded cardiac myocytes: a simulation study. *Biophys J* **78**, 2392–2404.
- Greenstein JL, Hinch R & Winslow RL (2006). Mechanisms of excitation-contraction coupling in an integrative model of the cardiac ventricular myocyte. *Biophys J* **90**, 77–91.
- Gaur N & Rudy Y (2011). Multiscale modeling of calcium cycling in cardiac ventricular myocyte: macroscopic consequences of microscopic dyadic function. *Biophys J* **100**, 2904–2912.
- Hadley RW & Hume JR (1987). An intrinsic potential dependent inactivation mechanism associated with calcium channels in guinea-pig myocytes. *J Physiol* **389**, 205–222.
- Hille B (2001). *Ion Channels of Excitable Membranes*, 3rd edn. Sinauer Associates, Inc. Sunderland, MA, USA.
- Heinzel FR, Bito V, Volders PG, Antoons G, Mubagwa K & Sipido KR (2002). Spatial and temporal inhomogeneities during Ca^{2+} release from the sarcoplasmic reticulum in pig ventricular myocytes. *Circ Res* **91**, 1023–1030.
- Hund TJ & Rudy Y (2004). Rate dependence and regulation of action potential and calcium transient in a canine cardiac ventricular cell model. *Circulation* **110**, 3168–3174.
- Higgins ER, Goel P, Puglisi JL, Bers DM, Cannell M & Sneyd J (2007). Modelling calcium microdomains using homogenisation. *J Theor Biol* **247**, 623–644.
- Kass RS & Sanguinetti MC (1984). Inactivation of calcium channel current in the calf cardiac Purkinje fiber. *J Gen Physiol* **84**, 705–726.
- Hofer GF, Hohenthanner K, Baumgartner W, Groschner K, Klugbauer N, Hofmann F & Romanin C (1997). Intracellular Ca^{2+} inactivates L-type Ca^{2+} channels with a Hill coefficient of approximately 1 and an inhibition constant of approximately 4 μM by reducing channel's open probability. *Biophys J* **73**, 1857–1865.
- Keller JB (1976). Inverse problems. *Am Math Monthly* **83**, 107–118.
- Kong H, Jones PP, Koop A, Zhang L, Duff HJ & Chen SRW (2008). Caffeine induces Ca^{2+} release by reducing the threshold for luminal Ca^{2+} activation of the ryanodine receptor. *Biochem J* **414**, 441–452.
- Jayasinghe ID, Cannell MB & Soeller C (2009). Organization of ryanodine receptors, transverse tubules, and sodium-calcium exchanger in rat myocytes. *Biophys J* **97**, 2664–2673.
- Langer GA & Peskoff A (1998). Calcium concentration and movement in the ventricular cardiac cell during an excitation-contraction cycle. *Biophys J* **74**, 153–174.
- Lee KS, Marban E & Tsien RW (1985). Inactivation of calcium channels in mammalian heart cells: joint dependence on membrane potential and intracellular calcium. *J Physiol* **364**, 395–411.
- Li P & Rudy Y (2011). A model of canine purkinje cell electrophysiology and Ca^{2+} cycling. *Circ Res* **109**, 71–79.
- Livshitz LM & Rudy Y (2007). Regulation of Ca and electrical alternans in cardiac myocytes: role of CAMKII and repolarizing currents. *Am J Physiol Heart Circ Physiol* **292**, H2854–H2866.

- Livshitz LM & Rudy Y (2009). Uniqueness and stability of action potential models during rest, pacing and conduction using problem solving environment. *Biophys J* **97**, 1265–1276.
- Luo CH & Rudy Y (1994). A dynamic model of the cardiac ventricular action potential. Simulations of ionic currents and concentration changes. *Circ Res* **74**, 1071–96.
- Mahajan A, Shiferaw Y, Sato D, Baher A, Olcese R, Xie L-H, Yang M-J, Chen P-S, Restrepo JG, Karma A, Garfinkel A, Qu Z & Weiss JN (2008). A rabbit ventricular action potential model replicating cardiac dynamics at rapid heart rates. *Biophys J* **94**, 392–410.
- Melzer W, Rios E & Schneider MF (1987). A general procedure for determining the rate of calcium release from the sarcoplasmic reticulum in skeletal muscle fibers. *Biophys J* **51**, 849–863.
- Morad M & Soldatov N (2005). Calcium channel inactivation: Possible role in signal transduction and Ca^{2+} signaling. *Cell Calcium* **38**, 223–231.
- Naraghi M & Neher E (1997). Linearized buffered Ca^{2+} diffusion in microdomains and its implications for calculation of $[\text{Ca}^{2+}]$ at the mouth of a calcium channel. *J Neuroscience* **17**, 6961–6973.
- Ottolia M, Nicoll DA & Philipson KD (2009). Roles of two Ca^{2+} -binding domains in regulation of the cardiac Na^+ – Ca^{2+} exchanger. *J Biol Chem* **284**, 32735–32741.
- Pasek M, Brette F, Nelson A, Pearce C, Qaiser A, Christe G & Orchard CH (2008). Quantification of t-tubule area and protein distribution in rat cardiac ventricular myocytes. *Prog Biophys Mol Biol* **96**, 244–257.
- Priori SG & Chen SR (2011). Inherited dysfunction of sarcoplasmic reticulum Ca^{2+} handling and arrhythmogenesis. *Circ Res* **108**, 871–883.
- Puglisi J, Yuan W, Bassani J & Bers DM (1999). Ca^{2+} influx through Ca^{2+} channels in rabbit ventricular myocytes during action potential clamp –Influence of temperature. *Circ Res* **85**, E7–E16.
- Post JA & Langer GA (1992). Sarcolemmal calcium binding sites in heart. I. Molecular origin in “gas-dissected” sarcolemma. *J Membr Biol* **129**, 49–57.
- Reeves JP & Condrescu M (2003). Allosteric activation of sodium–calcium exchange activity by calcium: persistence at low calcium concentrations. *J Gen Physiol* **122**, 621–639.
- Sato D, Shiferaw Y, Garfinkel A, Weiss JN, Qu Z & Karma A (2006). Spatially discordant alternans in cardiac tissue: Role of calcium cycling. *Circ Res* **99**, 520–527.
- Saucerman & Bers (2012). Calmodulin binding proteins provide domains of local Ca^{2+} signaling in cardiac myocytes. *J Mol Cell Cardiol* **52**, 312–316.
- Sipido KR & Wier WG (1991). Flux of Ca^{2+} across the sarcoplasmic guinea-pig cardiac cells during excitation–coupling. *J Physiol* **435**, 605–663.
- Sipido KR, Callewaert G & Carmeliet E (1995). Inhibition and rapid recovery of ICa during calcium release from the sarcoplasmic reticulum in guinea-pig ventricular myocytes. *Circ Res* **76**, 102–109.
- Shiferaw Y, Watanabe MA, Garfinkel A, Weiss JN & Karma A (2003). Model of intracellular calcium cycling in ventricular myocytes. *Biophys J* **85**, 3666–3686.
- Smyrniasi I, Maira W, Harzheima D, Walkera SAHL & Bootman MD (2010). Comparison of the T-tubule system in adult rat ventricular and atrial myocytes, and its role in excitation-contraction coupling and inotropic stimulation. *Cell Calcium* **47**, 210–223.
- Soeller C, Crossman D, Gilbert R & Cannell MB (2007). Analysis of ryanodine receptor clusters in rat and human cardiac myocytes. *Proc Natl Acad Sci U S A* **104**, 14958–14963.
- Soeller C, Jayasinghe ID, Li P, Holden AV & Cannell MB (2009). Three-dimensional high-resolution imaging of cardiac proteins to construct models of intracellular Ca^{2+} signalling in rat ventricular myocytes. *Exp Physiol* **94**, 496–508.
- Sham JSK (1997). Ca^{2+} release-induced inactivation of Ca^{2+} current in rat ventricular myocytes: Evidence for local Ca^{2+} signalling. *J Physiol* **500**, 285–295.
- Shannon TR, Wang F, Puglisi JL, Weber C & Bers DM (2004). A mathematical treatment of integrated Ca^{2+} dynamics within the ventricular myocyte. *Biophys J* **87**, 3351–3371.
- Standen NB & Stanfield PR (1982). A binding-site model for calcium channel inactivation that depends on calcium entry. *Proc R Soc Lond B Biol Sci* **217**, 101–110.
- Stengl M, Bartak F, Sykora R, Chvojka J, Benes J, Krouzecky A, Novak I, Svirglerova J, Kuncova J & Matejovic M (2010). Reduced L-type calcium current in ventricular myocytes from pigs with hyperdynamic septic shock. *Crit Care Med* **38**, 579–587.
- Stern MD (1992). Theory of excitation-contraction coupling in cardiac muscle. *Biophys J* **63**, 497–517.
- Trafford AW, Diaz ME, O’Neill SC & Eisner DA (1995). Comparison of subsarcolemmal and bulk calcium-concentration during spontaneous calcium-release in rat ventricular myocytes. *J Physiol* **488**, 577–586.
- Weber C, Piacentino V, Ginsburg K, Houser S & Bers DM (2002). Na^+ - Ca^{2+} exchange current and submembrane $[\text{Ca}^{2+}]$ during the cardiac action potential. *Circ Res* **90**, 182–189.
- Weber C, Ginsburg K, Philipson K, Shannon T & Bers DM (2001). Allosteric regulation of Na/Ca exchange current by cytosolic Ca in intact cardiac myocytes. *J Gen Physiol* **117**, 119–131.
- Winka LL, Sheng-Yong Wang & Langer GA (1999). Subcellular Ca^{2+} distribution with varying Ca^{2+} load in neonatal cardiac cell culture. *Biophys J* **76**, 2649–2663.
- Zahradnikova A, Kubalova Z, Pavelkova J, Gyorke S & Zahradnik I (2004). Activation of calcium release assessed by calcium release-induced inactivation of calcium current in rat cardiac myocytes. *Am J Physiol Cell Physiol* **286**, C330–C341.

Author contributions

L.L. participated in data analysis, provided the theoretical basis for the computations, and contributed to manuscript writing. K.A. performed experiments and data analysis and participated in manuscript writing. K.A. developed the computational methods together with L.L. and Y.R. G.A. performed experiments and data analysis and participated in manuscript writing. K.S. contributed to the experimental study design and the final manuscript writing. Y.R. participated in data

analysis, provided the theoretical basis for the computations, and participated in manuscript writing. All authors approved the final version of the manuscript. The experimental work was conducted at the laboratory in Leuven, Belgium, with additional analysis performed at the University of Szeged and at Washington University in St Louis.

Acknowledgements

This research was supported by the NIH–National Heart, Lung and Blood Institute Grants R01-HL049054-19 and R01-HL033343-27 (to Y.R.). This material is based upon

work supported in part by the National Science Foundation under Grant No. CBET-0929633. Any opinions, findings and conclusions or recommendations expressed in this material are those of the authors and do not necessarily reflect the views of the National Science Foundation (NSF). The work was also supported in part by the Fondation Leducq Award to the Alliance for Calmodulin Kinase Signalling in Heart Disease (to K.R.S. and Y.R.). Y.R. is the Fred Saigh Distinguished Professor at Washington University. This study was funded by grants from the Belgian Science Policy Program P6/31 and European Union grant Health-F2-2009-241526 EUTrigTreat (to K.R.S.).